

Can the symmetric *Fermi* and eROSITA bubbles be produced by tilted jets?

Po-Hsun Tseng

*Institute of Astrophysics, National Taiwan University, Taipei 10617, Taiwan and
Department of Physics, National Taiwan University, Taipei 10617, Taiwan*

H.-Y. Karen Yang

*Institute of Astronomy, National Tsing Hua University, Hsinchu 30013, Taiwan
Department of Physics, National Tsing Hua University, Hsinchu 30013, Taiwan and
Physics Division, National Center for Theoretical Sciences, Taipei 10617, Taiwan*

Chun-Yen Chen

Institute of Astrophysics, National Taiwan University, Taipei 10617, Taiwan

Hsi-Yu Schive

*Institute of Astrophysics, National Taiwan University, Taipei 10617, Taiwan
Physics Division, National Center for Theoretical Sciences, Taipei 10617, Taiwan
Department of Physics, National Taiwan University, Taipei 10617, Taiwan and
Center for Theoretical Physics, National Taiwan University, Taipei 10617, Taiwan*

Tzihong Chiueh

*Institute of Astrophysics, National Taiwan University, Taipei 10617, Taiwan
Physics Division, National Center for Theoretical Sciences, Taipei 10617, Taiwan and
Department of Physics, National Taiwan University, Taipei 10617, Taiwan*

The *Fermi* Gamma-Ray Space Telescope reveals two large bubbles in the Galaxy, extending nearly symmetrically $\sim 50^\circ$ above and below the Galactic center (GC). Previous simulations of bubble formation invoking active galactic nucleus (AGN) jets have assumed that the jets are vertical to the Galactic disk; however, in general, the jet orientation does not necessarily correlate with the rotational axis of the Galactic disk. Using three-dimensional special relativistic hydrodynamic simulations including cosmic rays (CRs) and thermal gas, we show that the dense clumpy gas within the Galactic disk disrupts jet collimation (“failed jets” hereafter), which causes the failed jets to form hot bubbles. Subsequent buoyancy in the stratified atmosphere renders them vertical to form the symmetric *Fermi* and eROSITA bubbles (collectively, Galactic bubbles). We find that (1) despite the relativistic jets emanated from the GC are at various angles $\leq 45^\circ$ with respect to the rotational axis of the Galaxy, the Galactic bubbles nonetheless appear aligned with the axis; (2) the edge of the eROSITA bubbles corresponds to a forward shock driven by the hot bubbles; (3) followed by the forward shock is a tangling contact discontinuity corresponding to the edge of the *Fermi* bubbles; (4) assuming a leptonic model we find that the observed gamma-ray bubbles and microwave haze can be reproduced with a best-fit CR power-law spectral index of 2.4; The agreements between the simulated and the observed multi-wavelength features suggest that forming the Galactic bubbles by oblique AGN failed jets is a plausible scenario.

I. INTRODUCTION

The detection of the *Fermi* bubbles [1, 54, 73], two large bubbles symmetrically extending about 50 degrees above and below the Galactic plane, is one of the great discoveries of the *Fermi* Large Area Telescope [4]. The gamma-ray emission of the *Fermi* bubbles is observed in the energy range of ~ 1 –100 GeV and has an almost spatially uniform hard spectrum, sharp edges, and an approximately flat brightness distribution (see reviews by Yang et al. 83 and Yang et al. 88). Recently, the newly launched eROSITA [63] conducted an all-sky X-ray survey with high sensitivities and revealed two gigantic bubbles (eROSITA bubbles hereafter) extending to ~ 80 degrees in Galactic latitudes, corresponding to an intrinsic size of 14 kpc across [62]. The remarkable resemblance between the eROSITA and *Fermi* bubbles suggests that they likely share the same origin [89]. Their symmetry about the GC further suggests that these Galactic bubbles may be generated by powerful energy injections from the GC, possibly related to nuclear star formation [13, 16, 17, 66] or past AGN activity [30, 31, 52, 84, 85, 87]. The latter scenario is what we will focus on in this work.

Previous attempts [30, 85, 90] to model the formation of the symmetric Galactic bubbles by AGN jets have typically assumed that the jets are vertical to the Galactic plane. While there are some observational indications of pc-scale jets from Sgr A* that are found to be perpendicular to the Galactic plane [42, 92], generally speaking, the AGN jet

orientation is determined by the black hole spin and the accretion disk in the black-hole vicinity and does not need to align with the rotational axis of the host galaxy. Indeed, observationally there is a lack of evidence for the alignment between AGN jets and the disk normal [e.g., 28]. The jets are often oblique to the disk normal (e.g. NGC 3079, Cecil et al. 14; NGC 1052, Dopita et al. 21), and there are even cases in which the jets lie in the plane of the disk (e.g., IC 5063, Morganti et al. 51).

To this end, the aim of this work is to remove the assumption on jet orientations in the AGN jet models by introducing a dense, thin interstellar medium (ISM) disk that can interact with the central oblique jet, in an attempt to resolve the symmetry problem of the Galactic bubbles. More specifically, we use three-dimensional special relativistic hydrodynamics (SRHD) simulations involving CR jet injections from the central supermassive black hole (SMBH) in the Galaxy to investigate whether the *oblique* jet scenario is able to produce the *symmetric* Galactic bubbles. We will verify whether the oblique jet model is consistent with the observed features of the Galactic bubbles, including the shape, surface brightness, and spectra of the *Fermi* bubbles [1] and microwave haze [2, 20].

This paper is organized as follows. In Section II, we describe the numerical techniques and initial conditions employed. In Section III, we first present characteristics of our simulated Galactic bubbles, and then discuss how the disk affects the formation of the bubbles. We compare the morphology and profiles of the simulated eROSITA bubbles with the observed X-ray map in Section IIIB, and present the simulated and observed multi-wavelength spectra of the *Fermi* bubbles in Section IIIC. Finally, the discussion and conclusion of our findings are given in Section IV and V, respectively.

II. METHODOLOGY

We use the GPU-accelerated SRHD adaptive-mesh-refinement (AMR) code GAMER-SR developed at the National Taiwan University (Schive et al. 2010, 2018; Tseng et al. 2021) to carry out the simulations of the Galactic bubbles formed by CR and relativistic-fluid injections from the GC.

The governing equations solving the special relativistic ideal fluid including CR advection, and dynamical coupling between the thermal gas and CRs without CR diffusion can be written in a succinct form as

$$\partial_t D + \partial_j (DU^j/\gamma) = 0, \quad (1a)$$

$$\partial_t M^i + \partial_j (M^i U^j/\gamma + p_{\text{total}} \delta^{ij}) = -\rho \partial_i \Phi, \quad (1b)$$

$$\partial_t \tilde{E} + \partial_j \left[(\tilde{E} + p_{\text{total}}) U^j/\gamma \right] = -\rho (U_j/\gamma) \partial_j \Phi, \quad (1c)$$

$$\partial_t (\gamma e_{\text{cr}}) + \partial_j (e_{\text{cr}} U^j) = -p_{\text{cr}} \partial_j U^j - p_{\text{cr}} \partial_t \gamma, \quad (1d)$$

where the five conserved quantities of gas D , M^i , and \tilde{E} are the mass density, the momentum densities, and the reduced energy density, respectively. The reduced energy density is defined by subtracting the rest mass energy density of gas from the total energy density of gas. γ and U^j are the temporal and spatial components of four-velocity of gas. ρ is the gas density in the local rest frame defined by D/γ . p_{gas} is the gas pressure. p_{cr} and e_{cr} are the CR pressure and CR energy density measured in the local rest frame, related by $p_{\text{cr}} = e_{\text{cr}}/3$. p_{total} is the sum of p_{gas} and p_{cr} . Φ is the gravitational potential, G is the gravitational constant, c is the speed of light, and δ^{ij} is the Kronecker delta notation. Throughout this paper, Latin indices run from 1 to 3, except when stated otherwise. The set of Eq. 1 is closed by using the Taub-Mathews equation of state [EoS; 45, 76] that approximates the exact EoS [75] for ultra-relativistically hot gases coexisting with non-relativistically cold gases. Note that (1) we simply replace p_{total} by p_{gas} in this paper as we have assumed $p_{\text{cr}} \ll p_{\text{gas}}$; (2) we use the Newtonian gravity as an approximation since the gravitational effects resulting from the kinetic/thermal energies within jet sources are relatively insignificant compared to the overarching gravitational potential of the Galaxy; (3) the term $-p_{\text{cr}} \partial_t \gamma$ in Eq. 1d is omitted from our implementation since the maximum fluid velocity across the simulation domain, $\gamma \sim 1.166$ — found at the jet source —, is near the lower limit of the Lorentz factor, rendering this term less significant in comparison to the term $-p_{\text{cr}} \partial_j U^j$.

GAMER-SR adopts a new SRHD solver [78], which significantly reduces numerical errors in non- and ultra-relativistic limits caused by catastrophic cancellations in the conversion between primitive (ρ , U^j , p) and conserved variables (D , M^j , \tilde{E}). GAMER-SR also adaptively and locally reduce the min-mod coefficient [78] within the failed patch group rarely occurring in the SRHD solver, new patches allocations, and ghost-zone interpolations. In this manner, we provide an elegant approach to avoid the use of pressure/density floor, which is unnatural but widely used in almost all publicly available codes.

In order to track the evolution of CRs injected by the AGN jets and make predictions of the non-thermal radiation they produce, we adopt the CR hydrodynamic formalism and model the CRs as a second fluid [93]. The approach is similar to previous works of [30] and [85], but generalized to CRs that couple with thermal gas moving with relativistic

speeds. The detailed implementations of CR in GAMER-SR and tests of algorithm can be found in Appendix B. In this approach, the CRs are treated as a single species without distinctions between CR electrons and protons, and the CR energy density e_{cr} is evolved according to Eq. 1d. The CRs are advected with the thermal gas and can have adiabatic compression and expansion with the gas. Also, we do not simulate the spectral evolution of the CRs and assume that the CR-to-gas pressure ratio is much less than 1 so that the contribution of CR pressure gradient to the momentum of the gas can be ignored (we will see that the ratio is around 0.005–0.15 throughout the simulations). Therefore, in the simulations we have neglected the cooling of CRs because it should have a negligible impact on the overall dynamics.

As stressed by Yang et al. [85], CR diffusion with a canonical diffusion coefficient of $\kappa \sim 3 \times 10^{28} \text{ cm}^2 \text{ s}^{-1}$ in the Galaxy has a minor effect on the overall morphology of the *Fermi* bubbles as it only acts to smooth the CR distributions on the scales of $l \sim \sqrt{\kappa t} \sim 0.3 (t/1\text{Myr}) \text{ kpc}$. Including anisotropic CR diffusion can also help to sharpen the edges of the bubbles due to interplay between the magnetic field and anisotropic CR diffusion with suppressed perpendicular diffusion across the bubble surface. As for the magnetic field, [87] has found that the magnetic field within the *Fermi* bubbles needs to be amplified to comparable values to the ambient field in order to reproduce the microwave haze emission. We thus directly adopt the exponential model for the magnetic field distribution in our calculation for the haze (see descriptions in Section II A). For the above reasons, we have ignored CR diffusion and the magnetic field in the simulations.

In our study, the simulation domain is $14 \times 14 \times 28 \text{ kpc}^3$ in size, slightly larger than the observed eROISTA bubbles, with the outflow boundary condition. The domain is resolved using the Cartesian coordinate system with the finest spatial resolution 0.4 pc, approximately 50 times smaller than a typical molecular cloud.

A. The Galactic halo and disk models

As a proof-of-concept study, we approximate conventionally axisymmetric stellar potential of Milky Way by a plane-parallel potential that is symmetric about the Galactic plane, $z = 0$, in the simulation domain. The plane-parallel potential is fixed throughout our simulations and given by

$$\Phi_{\text{total}}(z) = \Phi_{\text{bulge}}(z) + \Phi_{\text{halo}}(z), \quad (2)$$

where

$$\Phi_{\text{bulge}}(z) = 2\sigma_{\text{bulge}}^2 \ln \cosh \left(z \sqrt{\frac{2\pi G \rho_{\text{bulge}}^{\text{peak}}}{\sigma_{\text{bulge}}^2}} \right) \quad (3)$$

is the potential of an isothermal slab mainly contributed by stars around the Galactic bulge, and $\Phi_{\text{halo}}(z) = v_{\text{halo}}^2 \ln(z^2 + d_{\text{h}}^2)$ is a plane-parallel logarithmic dark halo potential. The plane-parallel geometry for the Galactic halo is a simplified assumption that allows us to focus on the interaction between the jets and the clump disk (Section II B). In reality, the Galactic halo distribution should also depend on the galactocentric radius, as adopted in previous jet simulations [e.g., 30, 65, 66, 89]. Thus, the choice of plane-parallel geometry balances reality and the specific scientific questions we seek to answer. The radial potential profile and the centrifugal forces introduced by the rotating Galaxy may somewhat modify the morphology of the bubbles wider than the Galactic bulge after the jets break out from the dense disk; modified jet parameters may be needed to match with the morphology of the observed bubbles. One should therefore be cautious when making comparisons with the previous simulations.

With the isothermal assumption and the condition of hydrostatic equilibrium within the total potential of the disk and halo, as well as pressure equilibrium between the isothermal disk and the halo gas, we can write down the steady-state gaseous density distribution as

$$\rho_{\text{isoDisk}}(z) = \rho_{\text{isoDisk}}^{\text{peak}} \exp \left[-\frac{\Phi_{\text{total}}(z)}{k_B T_{\text{isoDisk}}/m_p} \right] \quad (4a)$$

, if $|z| < z_0$,

$$\rho_{\text{atmp}}(z) = \rho_{\text{atmp}}^{\text{peak}} \exp \left[-\frac{\Phi_{\text{total}}(z)}{k_B T_{\text{atmp}}/m_p} \right] \quad (4b)$$

, otherwise,

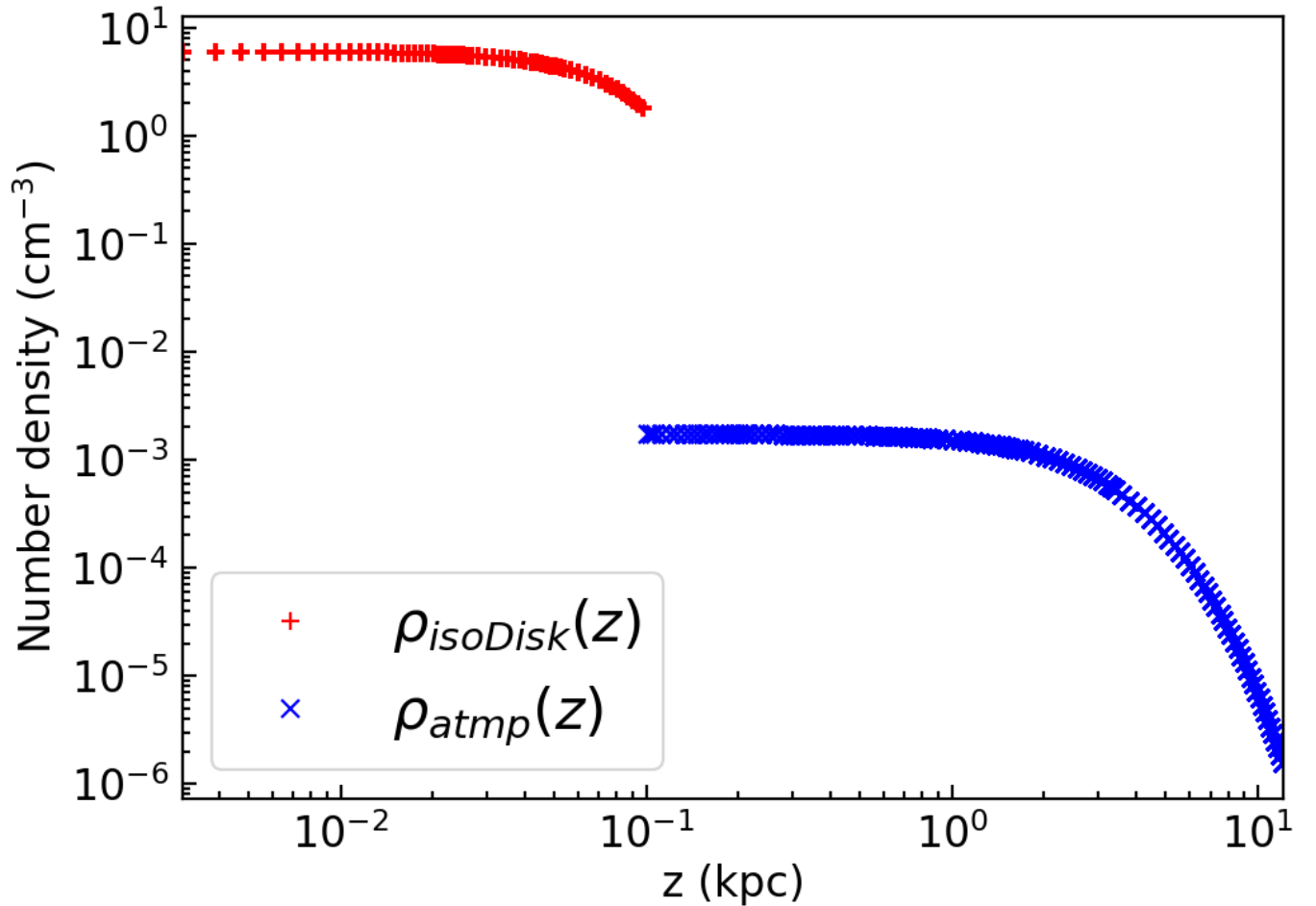


FIG. 1: The density profile of the isothermal disk (red pluses) and the ambient atmosphere (blue crosses) along the positive z -axis. The density distribution is derived from the condition of hydrostatic equilibrium. The gas at the interface between the isothermal disk and the atmosphere at $z = 0.1$ is in pressure equilibrium.

where m_p is the proton mass, T_{isoDisk} and T_{atmp} are the temperatures of the isothermal disk and the ambient atmosphere, and $\rho_{\text{isoDisk}}^{\text{peak}}$ and $\rho_{\text{atmp}}^{\text{peak}}$ are the peak density of the disk and the atmosphere at $z = 0$, respectively.

We tabulate parameters adopted for the Galactic model in Table I, except for $\rho_{\text{atmp}}^{\text{peak}}$ that can be derived from the other known parameters and the pressure equilibrium condition at the interfaces ($z = \pm z_0$) between the disk and the atmosphere. The density profile of Eq. 4 is shown in Fig. 1. Beyond the core radius (~ 2 kpc) the gas density decreases rapidly as a power-law.

To compute the predicted synchrotron radiation as a function of position, we adopt the default exponential magnetic field in GALPROP [72] that obeys the following spatial dependence:

$$|\mathbf{B}(R, z)| = B_0 \exp\left[-\frac{z}{z_0}\right] \exp\left[-\frac{R}{R_0}\right], \quad (5)$$

where $R = \sqrt{x^2 + y^2}$, B_0 is the average field strength at the GC, and z_0 and R_0 are the characteristic scales in the vertical and radial directions, respectively. We adopt $z_0 = 2$ kpc and $R_0 = 10$ kpc, which are best-fitting values in the GALPROP model to reproduce the observed large-scale 408 MHz synchrotron radiation in the Galaxy. We choose $B_0 = 50 \mu\text{G}$ based on the observed field strength at the GC [18].

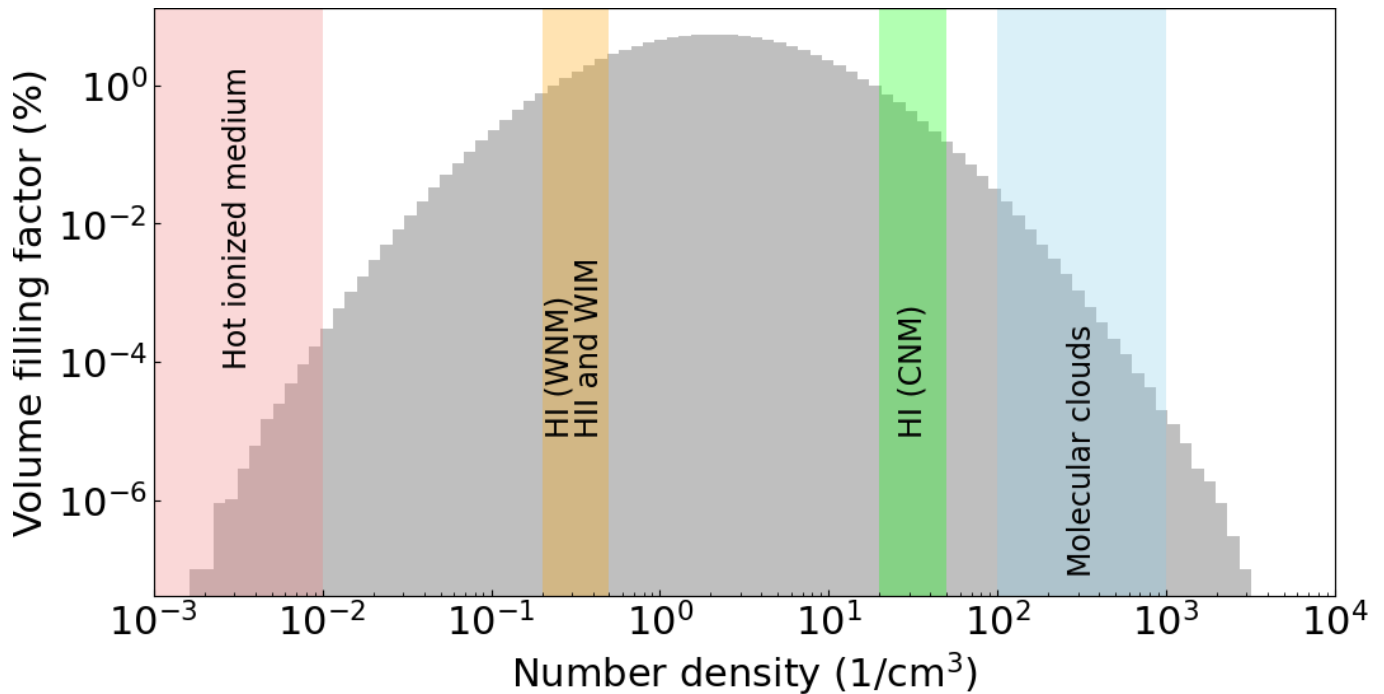


FIG. 2: The volume filling factor as a function of initial number density within the disk without the jet source. The vertical bands from left to right depict the allowable number densities [26] for hot ionized, warm neutral (WNM), warm ionized (WIM), cold neutral mediums (CNM), and molecular clouds.

B. The clumpy multiphase interstellar medium

A crucial component in our work is the clumpy ISM disk initialized by the publicly available pyFC code[55]. pyFC randomly generates a dimensionless 3D scalar field $f(\mathbf{x})$ that obeys the log-normal probability distribution with mean μ and dispersion σ , and follows the power-law Kolmogorov spectrum

$$D(\mathbf{k}) = \int k^2 \hat{f}(\mathbf{k}) \hat{f}^*(\mathbf{k}) d\Omega \propto k^{-\delta}, \quad (6)$$

where $\hat{f}(\mathbf{k})$ is the Fourier transform of $f(\mathbf{x})$. The spectrum $D(\mathbf{k})$ in the Fourier space is characterized by a power-law index $\delta = 5/3$, a Nyquist limit k_{\max} , and a lower cutoff wave number k_{\min} . k_{\max} is one-half of the spatial resolution within the disk, and k_{\min} is 375.0, corresponding to the maximum size of an individual clump of ~ 20 pc. Lewis & Austin [41] and Wagner et al. [82] have outlined a detailed procedure for constructing a clumpy scalar field, and we refer the readers for more information.

The density of the clumpy disk can then be obtained by taking the scalar products of $f(\mathbf{x})$ with $\rho_{\text{isoDisk}}(z)$ over all cells within the disk, i.e., $\rho_{\text{ismDisk}}(\mathbf{x}) = f(\mathbf{x})\rho_{\text{isoDisk}}(z)$. Also, the thermal pressure equilibrium within the clumpy disk implies that the temperature of the disk is $T_{\text{ismDisk}}(\mathbf{x}) = T_{\text{isoDisk}}(z)\rho_{\text{isoDisk}}(z)/\rho_{\text{ismDisk}}(\mathbf{x})$. The last category in Table I summarizes the parameters of the clumpy disk and their references.

On the basis of this setup, we cover the AMR base level with $16 \times 16 \times 32$ root cells, refined progressively on the mid-plane at $z = 0$ based on the gradient of density. We also restrict the refinement level at 7 within the disk so that a molecular cloud can be adequately resolved by approximately 30 cells along their diameter of 20 pc. We plot the volume filling factor as a function of initial number density within the disk without the jet source in Fig. 2, and show a close-up view of the pressure, temperature, and number density slices in the $y - z$ plane through the center of the disk in Fig. 3.

C. Oblique jets

We simulate the jets emanating from the GC with an inclination angle 45° with respect to the Galactic plane in order to alleviate the constraint that the jet direction must be perpendicular to the Galactic plane, and in particular

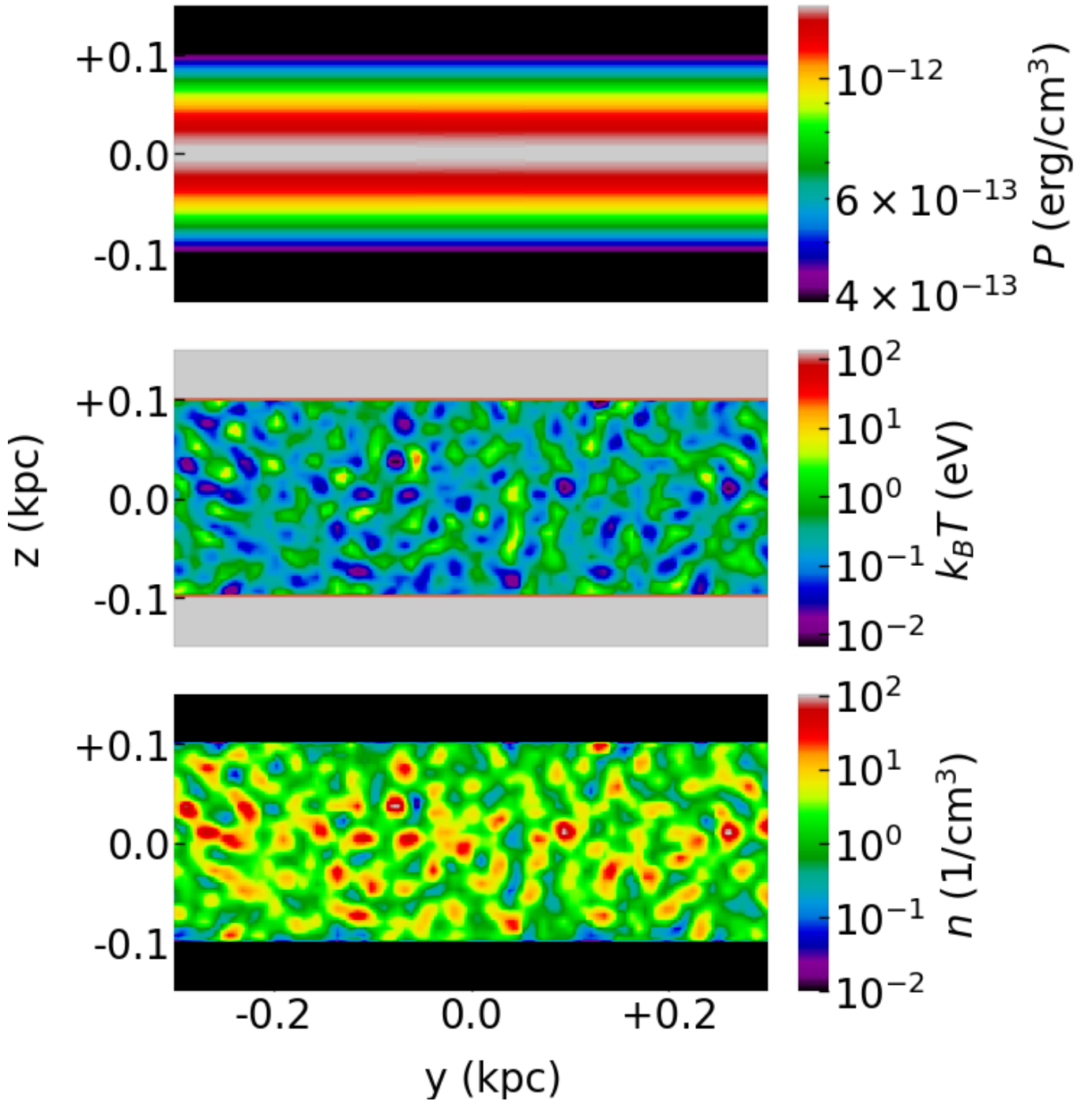


FIG. 3: Close-up view of the initial pressure (top), temperature (middle), and number density (bottom) slices in the $y - z$ plane through the center of the disk.

to investigate how the dense disk affects bubble formation.

We use the following quantities to characterize the jets: the flow four-velocity, $\beta\gamma = 0.6$; the gas density, $\rho_{\text{jet}} = 10^{-26}$ g/cm³; the gas temperature, $k_B T = 1.72$ MeV. This temperature corresponds to a gas pressure (p_{gas}) of 1.65×10^{-8} erg/cm³. Additionally, the CR pressure (p_{CR}) is set to 7.0×10^{-10} erg/cm³ (i.e., the initial CR-to-gas pressure ratio ~ 0.042). When compared to the surrounding medium, the density contrast between the thermal gas contained in the jet source and the ambient gas is $\rho_{\text{jet}}/\rho_{\text{amb}} = 10^{-3}$, and the temperature contrast is $T_{\text{jet}}/T_{\text{amb}} = 2 \times 10^4$. The jet power is thus 3.2×10^{42} erg s⁻¹, primarily driven by kinetic energy, with a kinetic-to-thermal energy ratio of 60.7 and an Eddington ratio of 0.008. Note that since we inject the jets at the center of the clumpy disk, we define the

TABLE I: Parameters of the disk, atmosphere, and gravitational potential in the simulations.

Parameter	Description	Value	Reference
Static stellar potential			
σ_{bulge}	Velocity dispersion of bulge	100 km s ⁻¹	[79]
$\rho_{\text{bulge}}^{\text{peak}}$	Peak average density of bulge	4×10^{-24} g cm ⁻³	N/A
Static dark halo potential			
v_{halo}	Characteristic velocity	131.5 km s ⁻¹	[34]
d_{h}	Core radius	12 kpc	"
Atmosphere			
T_{atmp}	Temperature of atmosphere	10 ⁶ K	[77]
Isothermal disk			
z_0	Scale height of disk	100 pc	[26]
T_{isoDisk}	Temperature of disk	10 ³ K	"
$\rho_{\text{isoDisk}}^{\text{peak}}$	Peak density of disk	10 ⁻²³ g cm ⁻³	"
Clumpy disk			
k_{min}^{\dagger}	Cutoff wave number	375.0	[26]
μ	Mean of scalar field	1.0	N/A
σ^{\ddagger}	Dispersion of scalar field	5.0	[25]
δ	Power law index	-5/3	N/A

\dagger $k_{\text{min}} = 375.0$ leads to the size of an individual molecular cloud of ~ 100 pc.

\ddagger In numerical simulations of turbulence, Federrath et al. [25] find $\sigma \sim 3.6$ and 35 for solenoidal (divergence-free) and compressive (curl-free) driving force, respectively, so that our adopted value of 5 is closer to their solenoidal result.

atmosphere gas density by the peak density of the isothermal disk on the mid-plane $z = 0$ (i.e. $\rho_{\text{isoDisk}}^{\text{peak}}$), as opposed to the *clumpy* density around the jet source.

The bipolar jets originate from the center of the simulation domain (i.e., active zones). The gas properties inside the jets are reset for each evolution time step; thus, the jets are constantly ejected from a cylindrical source starting from the beginning of the simulation ($t = 0$) and suddenly quenched at $t = 0.12$ Myr before fully breaking out the disk. Without quenching, the Galactic bubbles at the present time would be asymmetric about the Galactic plane. The diameter and height of cylindrical source are 4 pc, leading to a source volume (~ 50 pc³) much smaller than that of an individual clump by a factor of ~ 83 . By intentionally reducing the volume ratio of the jet source to an individual clump, we can mitigate the effect of the randomness of the clumps on the bubbles. Moreover, we resolve the jet source with the highest refinement level of 11, bringing the finest spatial resolution up to 0.4 pc.

The duration of the jets permits a total ejected energy of 1.2×10^{55} erg, which is 6–10 times lower than the estimated range of enclosed energy falling between 8×10^{55} erg and 1.3×10^{56} erg [62]. This discrepancy may arise from several assumptions involved in the observational constraint, such as the shape of the bubbles, thickness of the X-ray emitting shell, and the Mach number of the shock associated with the surface of eROSITA bubbles [62].

III. RESULTS

A. Morphology and properties of Galactic bubbles

Fig. 4a-4d show the slices of pressure (top), temperature (middle), and number density (bottom) from four different simulations, all ending at $t = 12.39$ Myr. The slices pass through the bipolar jet source tilted along $z = -y$ direction. Fig. 4a demonstrates the fiducial run with the initial condition specified in Section II shows that the edge of the outermost bubbles is a forward shock, expanding to 12.5 kpc above and below the Galactic plane, with a semiminor axis of about 6.8 kpc on the plane. The overall extent of the outermost bubbles is comparable to the two spherical objects of a radius of 6-7 kpc estimated by Predehl et al. [62] for modeling the eROSITA bubbles. The temperature profile (middle panel in the left column of Fig. 5) along the positive z -axis from the GC indicates that the temperature of the smooth region (purple band in Fig. 5) is around 0.3-0.5 keV, similar to 0.3 keV observed by Miller & Bregman [50] and Kataoka et al. [38].

Followed by the forward shock is a turbulent and hot plasma extending to a height of ~ 8 kpc (Fig. 5). The extent

of the turbulent plasma approximately agrees with that of the observed *Fermi* bubbles [74]. Also, the temperature of the plasma is around 2 keV, comparable to few keV inside the *Fermi* bubbles estimated by observing X-ray absorption lines through the hot gaseous halo along many different sight lines in the sky [49]. We also note that the turbulent, hot plasma is in pressure balance with the external medium, suggesting the outer edge of the *Fermi* bubbles is a contact discontinuity rather than a shock [90]. A 3D isocontour rendering of the temperature of the fiducial run is shown in Figure 6.

An interesting feature found in our simulations is that there are a pair of innermost bubbles (dashed box in the top panel of Fig. 4a) extending out from the GC on either side of the thin disk. The innermost bubbles are cold (1-10 eV), dense (10^{-4} – 10^{-2} cm $^{-3}$), and underpressured with respect to the turbulent plasma. The close-up view (right column in Fig. 5) of the vertical profiles and slices (Fig. 7) demonstrate that there is a sharp pressure jump at the edge of the innermost bubbles at $z = 3.62$ kpc, indicating that the innermost bubbles are an expanding reverse shock. The high-density upstream of the reverse shock requires an even higher density downstream. Continuing outward, there exists a dense shell before the gas density drops to values further downstream. The turbulent plasma is thus confined between the downstream of the reverse shock and the outermost forward shock, resulting in considerable heating of the turbulent plasma. These innermost bubbles are probably unrelated to the X-ray chimneys [60] and radio bubbles [32] due to their enormous difference in length (the total major-axis length of the X-ray chimneys and radio bubbles is 320 pc and 430 pc, respectively; however, the innermost bubbles is up to 4 kpc in length).

To show what are the key factors for reproducing the symmetry, we performed three additional simulations in different Galactic environments, shown in Fig. 4b-4d. Compared with the fiducial run (Fig. 4a), Fig. 4b differs by incorporating a smooth disk (the initial density profile is shown in Fig. 1) in the same atmosphere as the fiducial run, whereas Fig. 4c differs by using the smooth disk in a uniform atmosphere with a constant temperature $T_{\text{atmp}} = 10^6$ K and constant density $\rho_{\text{atmp}}(z = z_0)$. Fig. 4d varies by omitting the disk and adopting the stratified atmosphere described by Eq. 4b in the entire domain with a constant temperature $T_{\text{atmp}} = 10^6$ K. Note that all cases are initially in hydrostatic equilibrium since Fig. 4b and 4d adopt the same gravitational potential specified by Eq. 2 as the fiducial run. Fig. 4c also utilizes this potential, Eq. 2, for $|z| \leq z_0$, but for $|z| > z_0$, a flat potential is used.

We compare the clumpy disk (Fig. 4a) with the smooth disk in a stratified atmosphere (Fig. 4b), showing that the clumpiness of the dense disk has an insignificant effect on the overall dynamics of bubbles. However, the outermost bubbles arising from the smooth disk in a uniform atmosphere (Fig. 4c) is quasi-spherical, suggesting that the stratification facilitates the elongation of the outermost bubbles significantly. Fig. 4c and 4d reveal that the development of the innermost bubbles is always associated with the disk. Also, without the disk (Fig. 4d), the outermost bubbles and the turbulent plasma would be oblique, indicating that the dense disk is crucial for the production of symmetric Galactic bubbles.

B. Morphology and profiles in X-ray

The X-ray emissivity is computed for each computational cell using the MEKAL model [37, 43, 48] implemented in the utility XSPEC [3], assuming solar metallicity. The X-ray intensity map is then generated by projecting the emissivities along lines of sight pointing away from the solar position at $(R_{\odot}, 0, 0) = (8, 0, 0)$ kpc with angular resolutions of 0.5 degrees, where R_{\odot} is the Sun-GC distance. We do not account for any absorption effects, including free-free absorption and photoionization, because adequate modeling would require additional details, such as clumpiness and height of the Galactic disk. Modeling the exact properties of the Galactic disk is beyond the scope of our study and, therefore, is not included in our analysis. We point out that the projections used throughout this paper are ‘perspective’, which has the effect of making a distant object appear smaller than the same object at a closer distance, in order to facilitate a reliable interpretation of simulated all-sky map. Also, the observed X-ray emission is contributed by all the gas in the Milky Way halo, which likely extends to a radius of ~ 250 kpc [9, 29], much bigger than our simulation box. Therefore, we first compute the X-ray emissivity from the simulated gas within a radius of 25 kpc away from the GC. Then, beyond 25 kpc the gas is assumed to be isothermal with $T = 10^6$ K and follows the observed density profile of [77] out to a radius of 250 kpc.

Fig. 8a shows the comparison between the simulated (top) and observed (bottom) all-sky map in the range 0.6–1.0 keV. In the simulated map, the red arrow at the center represents the direction of the bipolar jets, constantly ejecting at an angle of 45° to the disk normal between 0–0.12 Myr. Fig. 8b displays the simulated X-ray photon count rates as a function of Galactic longitudes (red) in the same energy band as in Fig. 8a, cut at various Galactic latitudes (as labelled), compared with the observed profiles (black).

First, as shown in Fig. 4a, the full width of the outermost bubbles is around 14 kpc, corresponding to a full angular width $2 \sin^{-1}(7 \text{ kpc}/R_{\odot}) \sim 122^\circ$, which is as wide as the eROSITA bubbles in the simulated X-ray map (top panel in Fig. 8a). We therefore suggest that the eROSITA bubble shells are a signature of compressed forward shocks that have been driven into the northern and the southern Galactic halo, as previously proposed by Predehl et al. [62] and

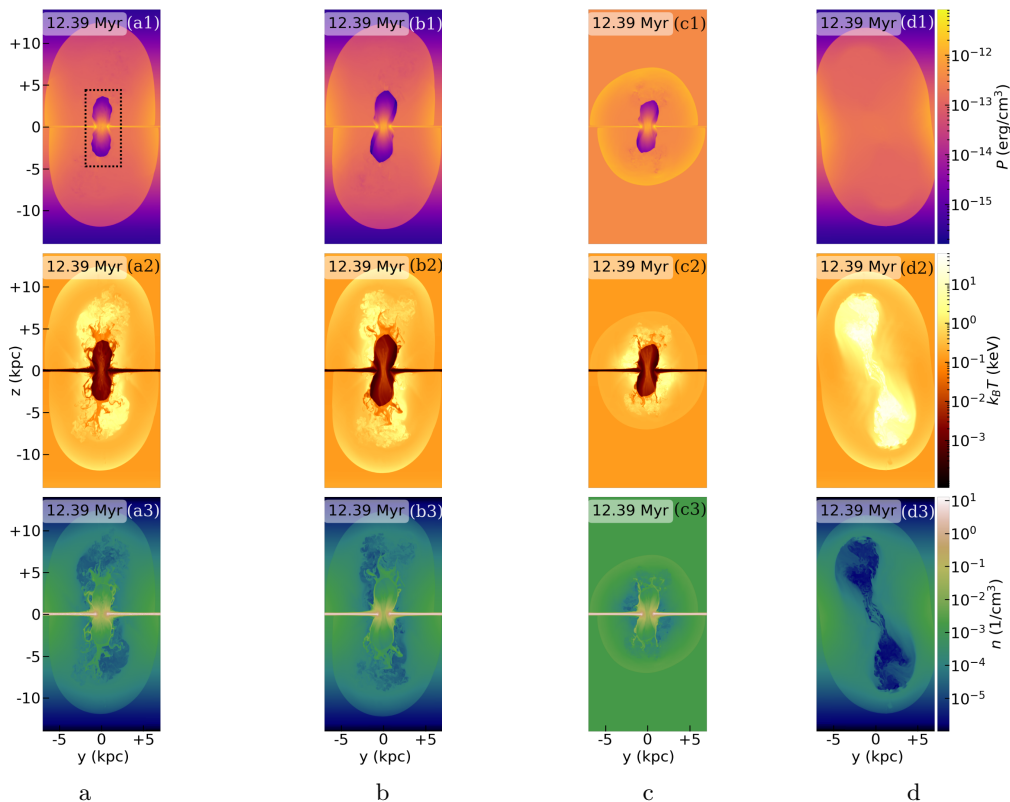


FIG. 4: The slices of pressure (top), temperature (middle), and number density (bottom) at the end of simulation $t = 12.39$ Myr. The slices pass through a bipolar jet source injecting along $z = -y$ direction for a duration $t = 0-0.12$ Myr. Comparison between the clumpy (Fig. 4a) and the smooth disks (Fig. 4b) in a stratified atmosphere shows that the initial density distribution of the dense disk has an insignificant effect on the overall dynamics of bubbles. However, the outermost bubbles arising from the smooth disk in a uniform atmosphere (Fig. 4c) are nearly spherical, suggesting that the stratification facilitates the elongation of the outermost bubbles significantly. Fig. 4c and 4d reveal that the development of the innermost bubbles is always associated with the disk. Also, without the disk (Fig. 4d), the outermost bubbles and the turbulent plasma would be oblique, indicating that the dense disk is crucial for the production of symmetric Galactic bubbles.

Yang et al. [89]. The broad agreement between simulated and observed X-ray maps hints that the full vertical extent of the eROSITA bubbles can be properly formed by an oblique jet within a thin disk of dense ISM.

Second, we observe that the simulated eROSITA bubbles are not as limb-brightened as the observed ones. A possibility to enhance the X-ray emission is to include shock-accelerated CRs near the shock, in which CRs could increase the compressibility of the fluid, resulting in the enhanced thermal Bremsstrahlung emissivity that is proportional to gaseous density squared. Also, the disagreement of the northeastern bubble is expected as the North Polar Spur, which is a giant ridge of bright X-ray emission that rises roughly perpendicularly out of the plane of the galaxy, might be a superposition of the GC structure and a remnant of the local supernova [6, 19, 57]. The North Polar Spur is not included in our simulations, whereas analyses based on X-ray data tend to suggest a GC origin [39, 40, 71].

Third, the innermost bubbles shown in Fig. 4, even though with high column density, are invisible in the simulated X-ray map as the temperature of the innermost bubbles is around 1–10 eV (see the temperature profile in Fig. 5). Consequently, the X-ray emission within the innermost bubbles is severely suppressed by the cutoff $\exp[-h\nu/k_B T]$ in the thermal Bremsstrahlung emissivity. This is the reason why the innermost bubbles are unseen in X-rays either through observations or simulations.

C. Gamma-ray and microwave spectra: constraint on the CRe spectral index

In this section, we obtain the constraint on the CRe spectral index by comparing the simulated gamma-ray and microwave spectra with the observed spectra of the *Fermi* bubbles [1] and the microwave haze [20], respectively.

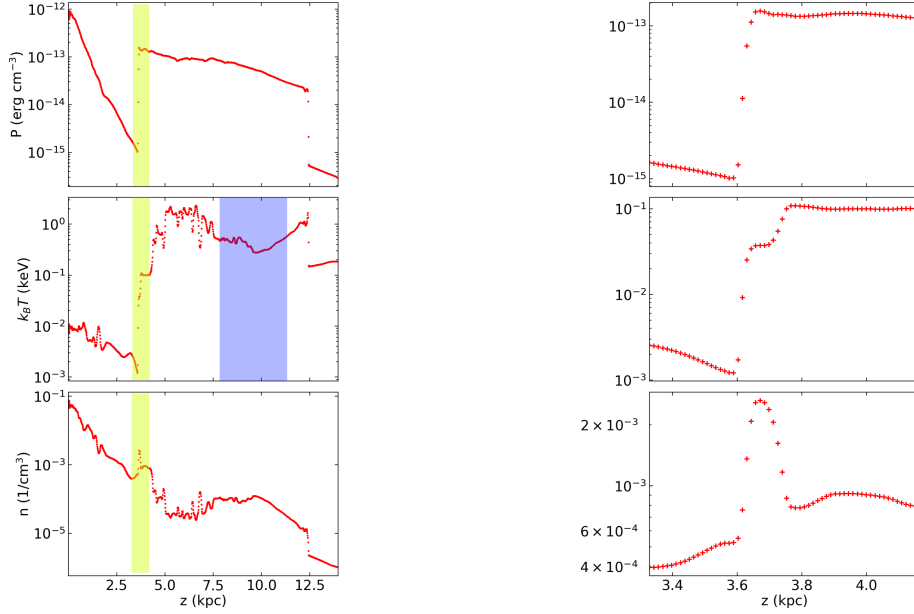


FIG. 5: Left: the profiles of pressure (top), temperature (middle), and number density (bottom) along the positive z -axis in Fig. 4. Right: the close-up view of the profiles in the yellow band. The sharp pressure jump at $z = 3.62$ kpc indicates that the innermost bubbles (dashed box in the top panel in Fig. 4a) are an expanding reverse shock.

We assume the leptonic model for the gamma-ray and microwave emission as previous studies have shown that the bubble and haze spectra can be simultaneously produced by the same population of CRe [1, 74, 87, 89]. In the leptonic scenario, the gamma-ray and microwave emission come from inverse-Compton (IC) scattering of the interstellar radiation field (ISRF) and synchrotron radiation, respectively. Because the evolution of CR spectrum is not modeled in the simulations, we assume that the CRe spectrum follows a power-law distribution:

$$N(\gamma_e) = \mathbb{C} \gamma_e^{-p_e}, \quad (7)$$

where γ_e is the Lorentz factor of the CRe; p_e is the spectral index of the CRe, assumed to be spatially uniform across the space. Since $N(\gamma_e)$ denotes the number of CRe per unit volume within energy range γ_e to $\gamma_e + d\gamma_e$, the normalization constant, denoted as \mathbb{C} , can be derived as follows:

$$\mathbb{C} = \begin{cases} \frac{e_{\text{cr}}}{m_e c^2} \left(\frac{2 - p_e}{\gamma_{e,\text{max}}^{2-p_e} - \gamma_{e,\text{min}}^{2-p_e}} \right), & p_e \neq 2, \\ \frac{e_{\text{cr}}}{m_e c^2} \left[\ln \left(\frac{\gamma_{e,\text{max}}}{\gamma_{e,\text{min}}} \right) \right]^{-1}, & p_e = 2, \end{cases} \quad (8)$$

where c is the speed of light, m_e is the electron mass, and $\gamma_{e,\text{max}}$ and $\gamma_{e,\text{min}}$ are the maximum and minimum Lorentz factor of the CRe, respectively. We stress that the normalization constant varies with space and time since \mathbb{C} is a function of e_{cr} governed by Eq. (1d). We assume that the CRe spectrum, Eq. (7), ranges from 0.5 MeV ($\gamma_{e,\text{min}} \sim 1$) to 562.1 GeV ($\gamma_{e,\text{max}} \sim 1.1 \times 10^6$), where $\gamma_{e,\text{max}}$ is motivated by the observed cutoff gamma-ray energy shown in Fig. 9 as most of the CRe energy is carried away by the up-scattered photons in the Klein-Nishina limit.

The IC emissivity of the upscattered photons at the energy ϵ_1 is computed for each computational cell in our simulations using the Klein-Nishina IC cross-section [10, 35] to handle the scattering between ultra-relativistic CRe and photons in the ISRF:

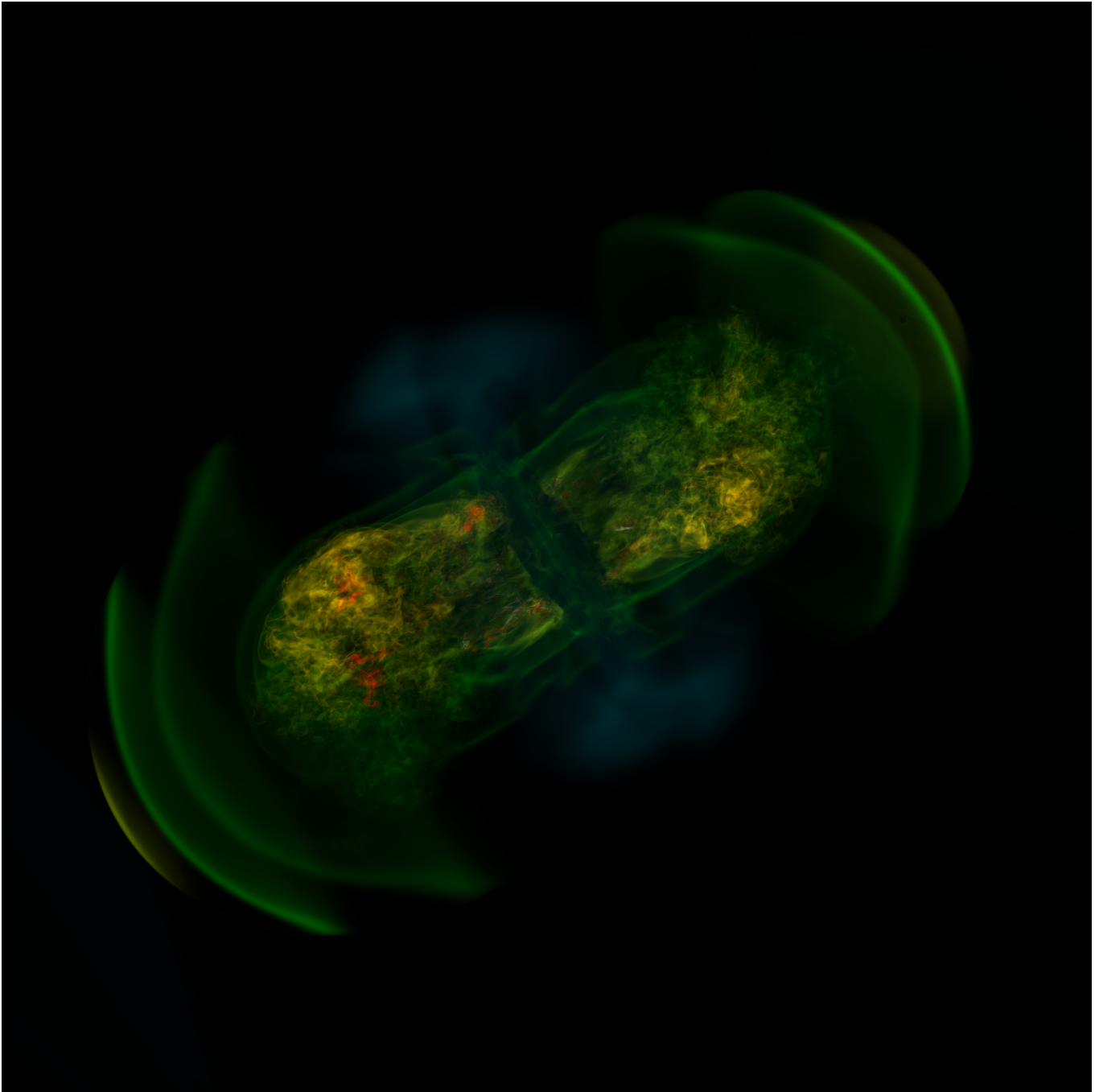


FIG. 6: A 3D isocontour rendering of the temperature of the fiducial run at the present time, indicating a turbulent, hot inner structure (*Fermi* bubbles) surrounded by a smooth, warm outer shell (eROSITA bubbles).

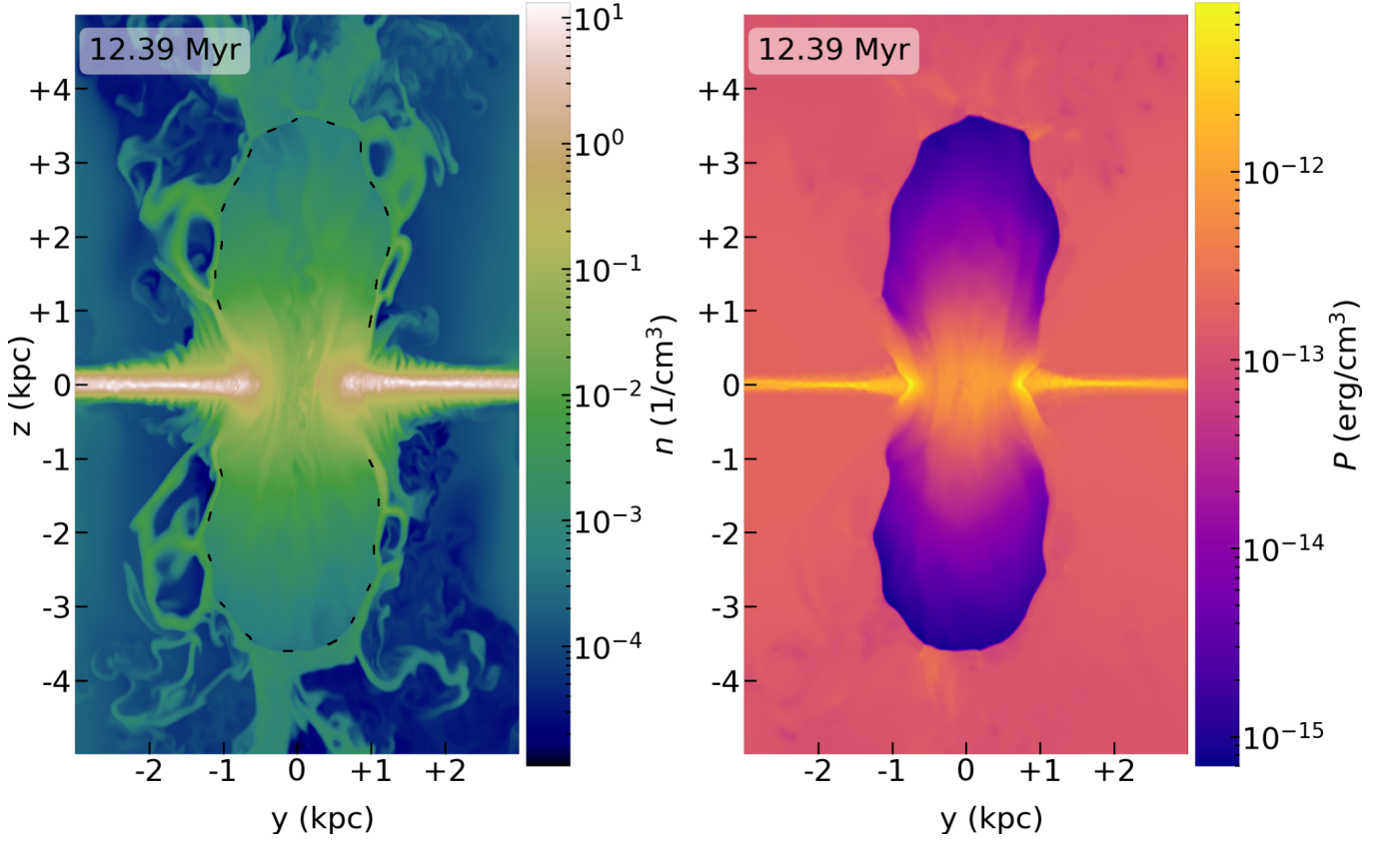


FIG. 7: Zoom-in images of the density (left) and pressure (right) slices of the innermost bubbles. The high density upstream of the reverse shock requires an even higher density downstream. Continuing outward, the higher density must match with low density further downstream; thus there exists a dense shell (the turbulent region outside the black dashed line in the left panel).

$$\frac{dE}{dt d\epsilon_1 dV} = \frac{3}{4} \sigma_T c C \epsilon_1 \int_{\epsilon_{\min}}^{\epsilon_{\max}} \frac{n(\epsilon)}{\epsilon} d\epsilon \int_{\gamma_{e,\min}(\epsilon)}^{\gamma_{e,\max}} \gamma_e^{-(p_e+2)} f(q, \Gamma) d\gamma_e, \quad (9a)$$

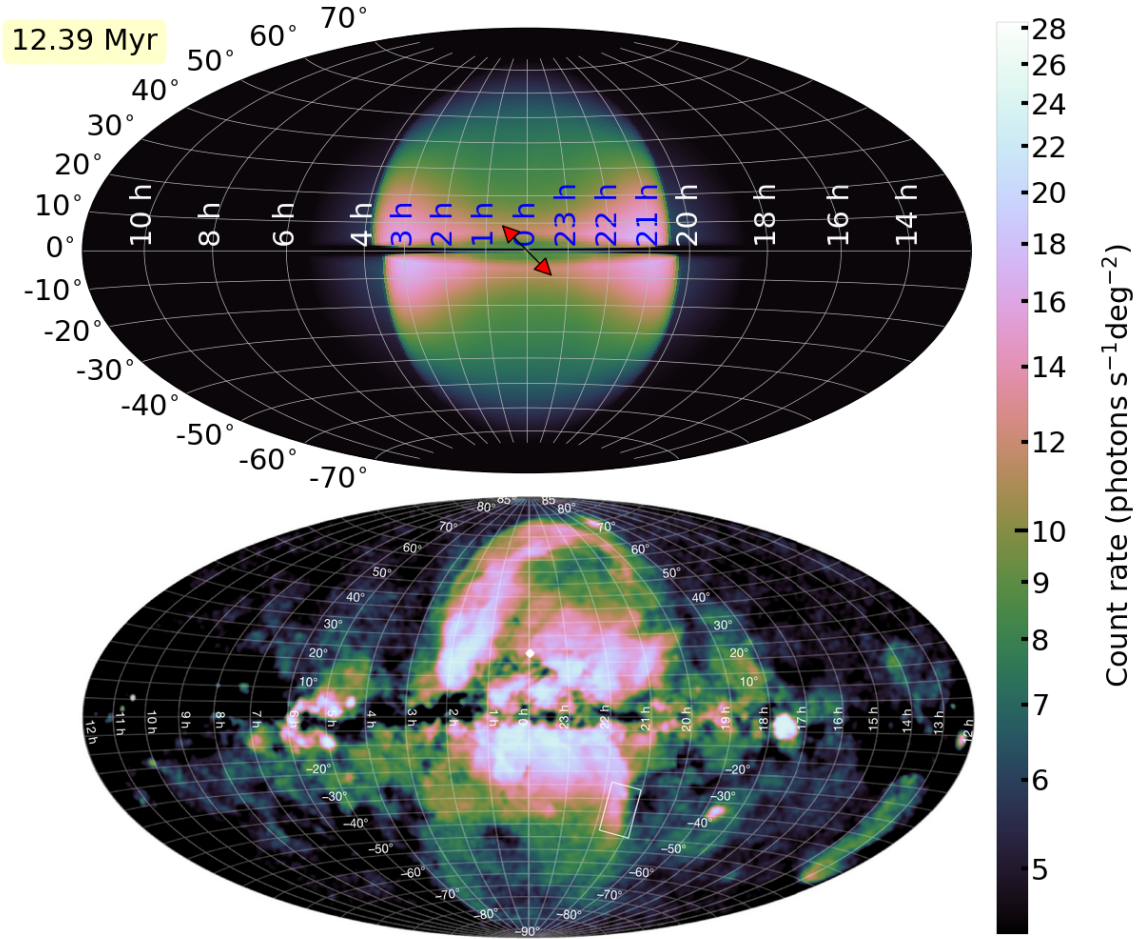
$$f(q, \Gamma) = 2q \ln q + (1 + 2q)(1 - q) + 0.5(1 - q) \frac{(\Gamma q)^2}{1 + \Gamma q}, \quad (9b)$$

$$q = \frac{\epsilon_1 / \gamma_e m_e c^2}{\Gamma (1 - \epsilon_1 / \gamma_e m_e c^2)}, \quad (9c)$$

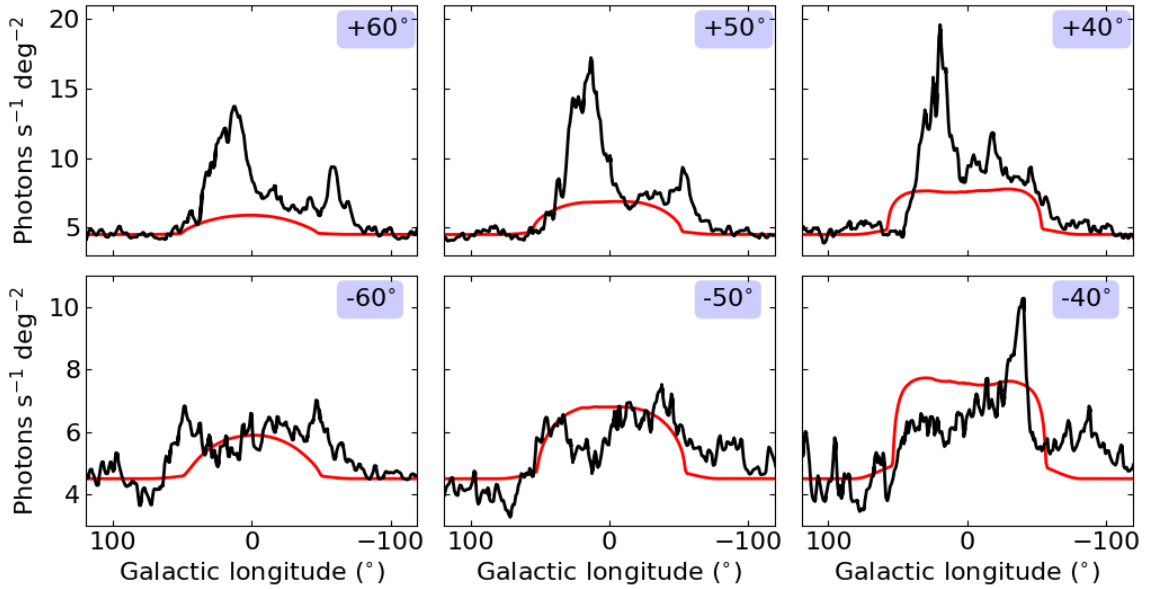
$$\Gamma = \frac{4\epsilon \gamma_e}{m_e c^2}, \quad (9d)$$

$$\gamma_{e,\min}(\epsilon) = 0.5 \left(\frac{\epsilon_1}{m_e c^2} + \sqrt{\left(\frac{\epsilon_1}{m_e c^2} \right)^2 + \frac{\epsilon_1}{\epsilon}} \right), \quad (9e)$$

where σ_T is the Thomson cross section; $\gamma_{e,\min}(\epsilon)$ is the minimum Lorentz factor of CRe that allows the incident photons to be scattered from energy ϵ to ϵ_1 ; $n(\epsilon)$ is the energy distribution of the photon number density in the ISRF given by Porter et al. [61], and this distribution varies depending on the Galactic location. To obtain the simulated IC emissivities, we perform the double integration in Eq. 9 on each cell over the range of the CRe Lorentz factor and



(a) Simulated (top) and observed (bottom; Predehl et al. 62) count rate (photons $s^{-1} \text{deg}^{-2}$) in the 0.6–1.0 keV range. Throughout this paper we show sky maps in Galactic coordinates centered on the Galactic center using a Hammer-Aitoff projection. The red arrow at the center of the top panel depicts the direction of the bipolar jets, constantly ejecting at an angle of 45° to the disk normal for the first 0.12 Myr.



(b) Comparison of the simulated (red) and observed (black; Predehl et al. 62) one-dimensional photon count-rate profiles in the same energy band as in Fig. 8a, cut at various Galactic latitudes (as labelled).

FIG. 8

the range of incident photon energy between $\epsilon_{\min} = 1.13 \times 10^{-4}$ eV (cosmic microwave background) and $\epsilon_{\max} = 13.59$ eV (optical starlight).

The synchrotron emissivity with an isotropic electron pitch angle distribution is given by Blumenthal & Gould [10]:

$$\frac{dE}{dt d\nu dV} = \frac{4\pi \mathbb{C} e^3 B^{0.5(p_e+1)}}{m_e c^2} \left(\frac{3e}{4\pi m_e c} \right)^{0.5(p_e-1)} a(p_e) \nu^{-0.5(p_e-1)}, \quad (10a)$$

$$a(p_e) = \frac{2^{0.5(p_e-1)} \sqrt{3} \Gamma[(3p_e-1)/12] \Gamma[(3p_e+9)/12] \Gamma[(p_e+5)/4]}{8\sqrt{\pi} (p_e+1) \Gamma[(p_e+7)/4]}, \quad (10b)$$

where Γ is the gamma function, and B is the magnetic field strength defined in Eq. 5. For a given longitude and latitude range, the simulated spectra are computed by projecting emissivities as we project X-ray emissivities in Section III B, and then we average the spectra over all the sight lines within a region in the sky.

Fig. 9 shows the simulated microwave (left) and gamma-ray (right) spectra averaged over the different patches (shown in legends) of the sky. The rows from top to bottom show the simulated spectra with different assumptions of the CRe spectral index (p_e) 2.2, 2.4, and 2.6. To fit the observed spectra, the CRe energy density (e_{cr}) at the end of the simulation ($t = 12.39$ Myr) is scaled by a factor of 0.17, 1.00, and 8.30 for p_e of 2.2, 2.4, 2.6, respectively, across the entire simulation domain. Given that Eq. 1d is linear to the CRe energy density, scaling the CRe energy density is reasonable provided that the resulting CRe pressure remains below the gas pressure throughout the simulation, which we verified to be true.[56]

We highlight our findings as follows. First, we find that, among the three values of the CR spectral indices assumed, a CRe spectral index of 2.4 (the middle row) provides the best fits to both the observed gamma-ray and microwave spectra. This value is slightly steeper than the best-fit spectral index of ~ 2.17 found by [1]. However, we note that our calculations takes into account the 3D variations of the ISRF, whereas the previous constraint was based on the ISRF at a fixed height of 5 kpc from the Galactic plane. On the other hand, the case with a spectral index of 2.2 provides acceptable fits to the gamma-ray spectrum and the slope of the microwave spectrum, but it falls short to reproduce the normalization of the microwave spectrum. This discrepancy could be resolved if the true magnetic field strength within the *Fermi* bubbles is slightly higher than that in the halo, or possibly considering the contribution from secondary CR electrons generated by a subdominant CR proton component. If that were the case, a spectral index of 2.2 would still be plausible.

Second, the simulated gamma-ray spectra are nearly latitude-independent. Note that we have assumed a spatially uniform spectrum for the underlying CRe, and hence the simulated gamma-ray spectra at different latitudes mainly reflect how the 3D distribution of the simulated CR number density (see Fig. 11) is projected into different latitude bins. Overall we find good agreement between the simulated and observed spectra [1]; only the simulated spectrum at high latitudes tends to be slightly dimmer than the lower-latitude spectrum because the optical intensity in the ISRF decays with increasing latitudes.

Third, our assumed range for the CRe spectrum (0.5 MeV to 562.1 GeV) produces gamma-ray spectra with a high-energy cutoff around energies 400–500 GeV, consistent with the observed cutoff energy. This is expected since the upscattered high-energy photons ($\epsilon_1 \sim 450$ GeV) mainly arise from the scattering between the relativistic CRe ($\gtrsim 408$ GeV) and optical starlight ($\epsilon \sim 10$ eV). Thus, Eq. 9e can be reduced to $\epsilon_1 \sim \gamma_e m_e c^2$ in the Klein–Nishina limit (i.e. $\epsilon_1 \epsilon \gg (m_e c^2)^2$), implying most of the CRe energy is carried away by the upscattered photons.

Finally, the good agreement between the simulated and observed gamma-ray/microwave spectra implies that, in the presence of ISRF and magnetic fields, the emission of the *Fermi* bubbles and the microwave haze can be produced by the same high-energy electrons via IC scattering and synchrotron radiation, respectively. Our results thus provide further support for the leptonic model as previously suggested [1, 74, 87, 89].

Fig. 10 shows the simulated gamma-ray photon flux with a CRe power-law index 2.4 compared with the observed one in the energy bin 76.8 – 153.6 GeV. As the eROSITA bubbles, one can see that the symmetric *Fermi* bubbles can also be realized by oblique jets. The extent of the simulated gamma-ray bubbles is also comparable to the observed ones. However, we find that the simulated bubble surface is not as smooth as the observed bubbles. The instabilities at the bubble surface may be suppressed by the magnetic draping effect [44, 85] if magnetic fields were included in the simulations. With magnetic draping, the sharp edges of the observed bubbles [1, 74] could also be explained by anisotropic CR diffusion along field lines [87].

As can be seen in Fig. 10, though the overall size of the simulated gamma-ray bubbles is comparable to that of the observed ones, the gamma-ray intensity does not appear to be as uniform as originally found in Su & Finkbeiner

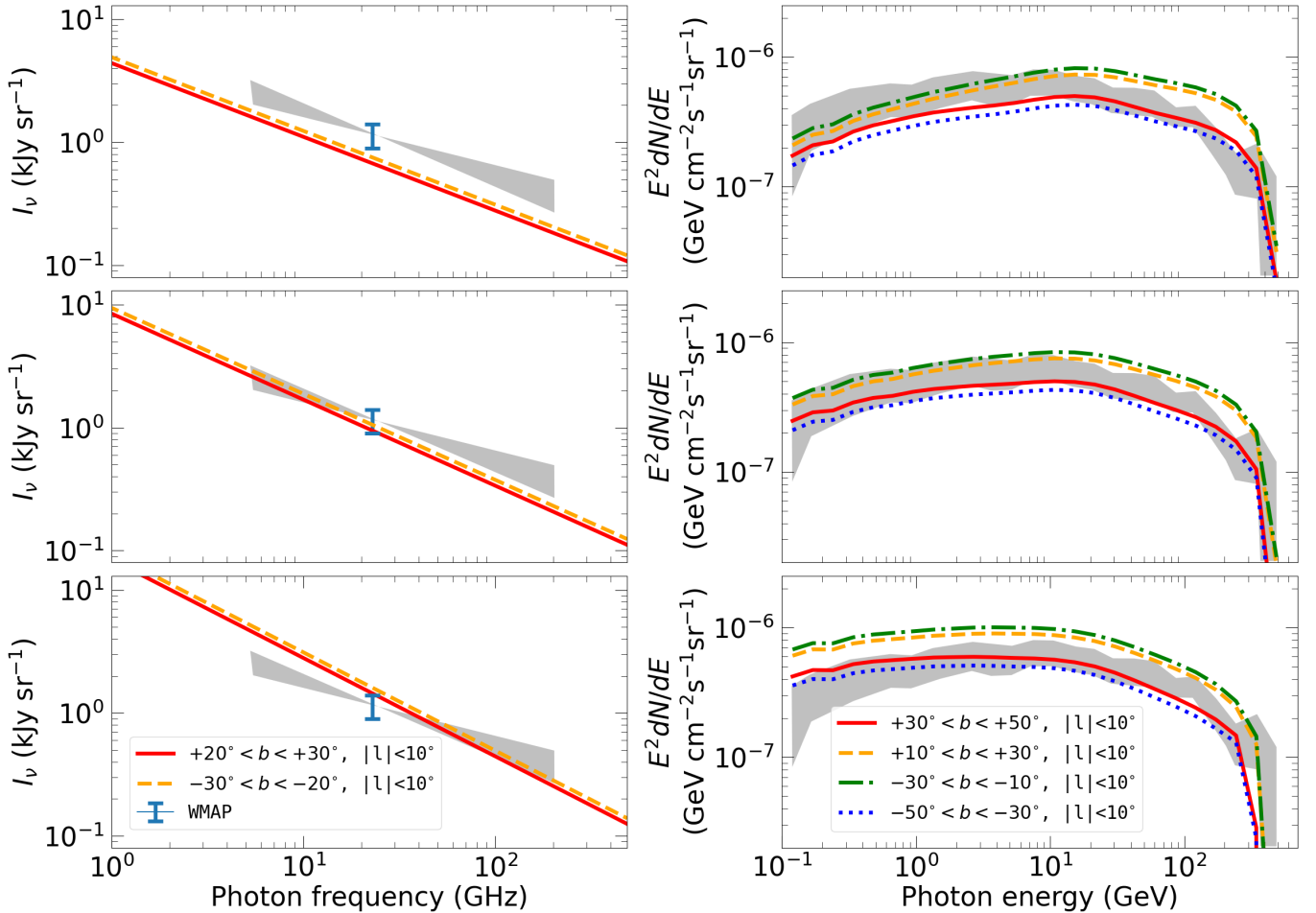


FIG. 9: Simulated microwave spectra (colored lines in left) averaged over $20^\circ < |b| < 30^\circ$, $|l| < 10^\circ$. The data point represents the *WMAP* data in the 23 GHz K band and the shaded bow-tie area indicates the range of synchrotron spectral indices allowed for the *WMAP* haze [20]. Simulated gamma-ray spectra (colored lines in right column) of the *Fermi* bubbles calculated for a longitude range of $|l| < 10^\circ$ for different latitude bins. The gray band represents the observational data of Ackermann et al. [1]. The row from top to bottom shows the microwave (left) and gamma-ray (right) spectra with CRe spectral index 2.2, 2.4 and 2.6, respectively. The CRe cutoff energy is 562.1 GeV in all cases.

[73]. As discussed above, the gamma-ray intensity is slightly higher close to the Galactic plane due to the stronger radiation field at lower latitudes. However, this level of brightness variations appears to be consistent with the later observational data of Ackermann et al. [1] and Selig et al. [69], which shows that there are some substructures in the gamma-ray intensity distribution within the bubbles.

For completeness, we show the simulated CR energy density at 12.39 Myr in Fig. 11. The comparison between Fig. 4 and Fig. 11 shows that the CR pressure is around $5 \times 10^{-16} - 10^{-14}$ erg cm $^{-3}$, corresponding to a CR-to-gas pressure ratio of 0.005–0.1, similar to 0.15 at the beginning of the simulation. We therefore stress that ignoring the contribution of CR pressure gradient to the momentum of the gas in Eq. 1 is reasonable.

IV. DISCUSSION

The success of the model hinges on the major assumption that the tilted jets dissipate almost all their kinetic energy within the cold ISM disk without directly penetrating through it. To find an optimal parameter set satisfying this assumption, we explore jet parameters, such as density, velocity, and temperature at varying jet tilt angles of 0° , 45° , and 90° , as detailed in the Appendix A. The findings indicate that 1) higher jet density and velocity cause the jets to penetrate the disk and form asymmetric bubbles; 2) lower jet density and velocity result in cooler post-shock

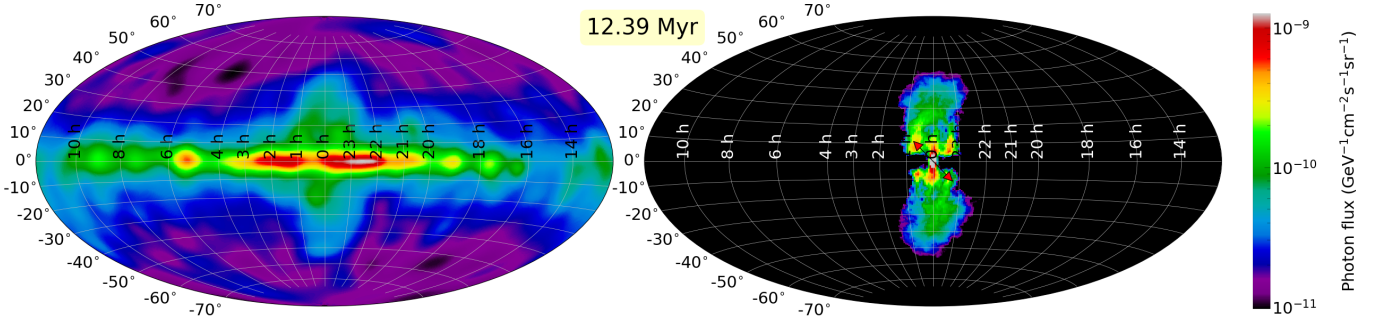


FIG. 10: The observed (left; Selig et al. 69) and simulated (right) photon flux in the energy bin $76.8 - 153.6$ GeV. Note that the left panel is the photon flux of the diffuse component reconstructed by the D³PO algorithm [69] that analyzes the photon data from the *Fermi* Large Area Telescope [4] and removes the contribution from point-like component. The red arrow at the center of the right panel depicts the direction of the bipolar jet, constantly ejecting at an angle of 45° to the disk normal in the first 0.12 Myr of the simulation.

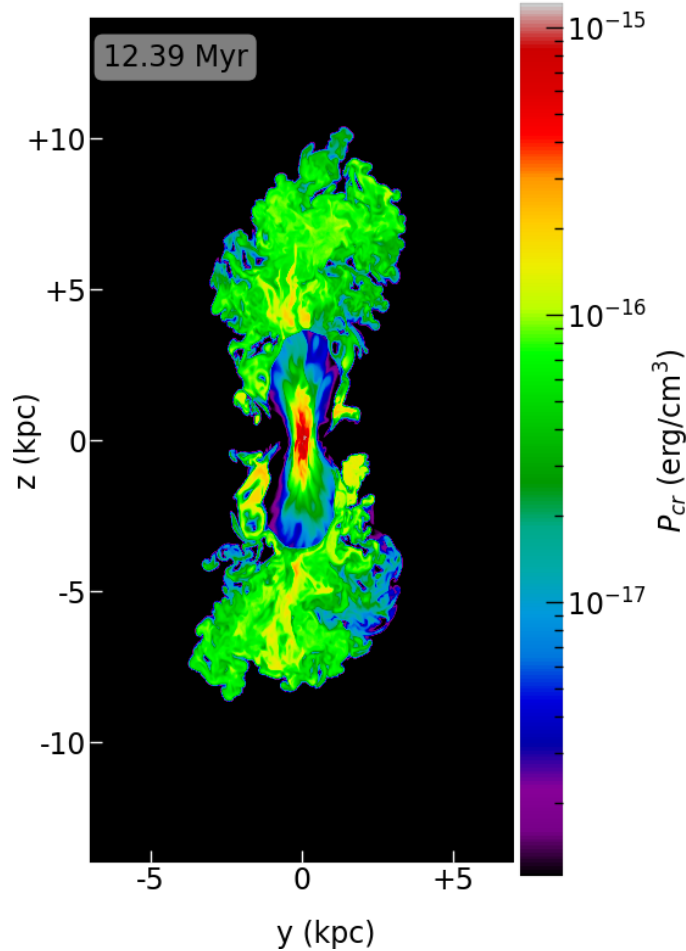


FIG. 11: The CR pressure slice passing through the jet source at 12.39 Myr. Comparison between gas pressure (Fig. 4) and cosmic ray pressure shows that the CR pressure is around $5 \times 10^{-18} - 10^{-16}$ erg cm^{-3} , bringing the CR-to-gas pressure ratio is $5 \times 10^{-5} - 10^{-3}$. We therefore stress that ignoring the contribution of CR pressure gradient to the momentum of the gas in Eq. 1 is reasonable.

regions, inconsistent with observations; 3) alternating the jet temperature — increasing it leads to hotter post-shock regions, while decreasing it results in cooler ones — also yields results that are inconsistent with observations; 4) both lying and vertical jet orientations produce dimmer γ -ray bubbles at high latitudes than the observed ones. The ideal jet parameters emerged as a temperature of $k_B T = 1.72$ MeV, a density of $\rho = 10^{-26}$ g/cm³, and a four-velocity of $\beta\gamma = 0.6$ at 45° inclination. Note that these optimal parameters are derived by assuming a clumpy cold disk with a constant half-height of $z_0 = 100$ pc; however, the actual disk height may vary with the distance to the Galactic center. Closer to the GC, the cold disk is even thinner – the half-height of the central molecular zone is about 30 pc, and the central circumnuclear gaseous disk may be even thinner. Under these conditions, it may be easier for the jets to penetrate through the cold disk, producing tilted *Fermi* and eROSITA bubbles inconsistent with observations; a lower jet density or velocity may be needed to remedy such cases.

Our modeled gamma-ray and microwave spectra assumed that the underlying CRe spectrum is spatially uniform with a spectral index of 2.4; however, the high energy CRe should severely suffer from synchrotron and IC losses, during their passage through the magnetic and radiation fields, respectively, within the Galaxy. The typical synchrotron and IC cooling time scale of high energy (~ 100 GeV) CRe in the Milky Way is ~ 1 Myr [84], ten times shorter than the formation time of 12 Myr as suggested by our simulations. Therefore, the CRe generating the gamma-ray emission would need to be re-accelerated by in-situ acceleration mechanisms such as shocks or turbulence. Since the forward shock is rather far away from the gamma-ray bubbles, re-acceleration is more likely associated with turbulence [46, 47], possibly in balance with the IC and synchrotron cooling. We will investigate the competition between stochastic acceleration and radiative cooling in future work. Overall, our results imply that in the oblique-jet scenario, regardless of what the true re-acceleration and cooling mechanisms are, the CRe spectrum at the present time has to be spatially uniform with a spectral index of 2.4 in order to fit the observed spectra.

Recent simulations by [65] and [22] have also investigated the oblique-jet scenario in terms of generating the Galactic bubbles. Our results agree with their findings that, in the oblique-jet scenario, the jets must have significant dissipation within the Galactic disk in order to produce symmetric Galactic bubbles as the observed ones. However, they found that only jets with super-Eddington power ($L_j \gtrsim 5 \times 10^{44}$ erg s⁻¹) could dissipate sufficient energy and produce symmetric bubbles, while lower-power jets tend to penetrate the disk and produce asymmetric bubbles. In contrast, our simulations show that relatively low-power jets ($L_j = 3.2 \times 10^{42}$ erg s⁻¹) could still dissipate a significant amount of energy before leaving the disk and generate symmetric bubbles as observed (see also [53] or M18). In the Appendix of [65], they attributed their different results from M18 to numerical resolution. However, our resolution is ~ 10 times greater and we still find significant jet dissipation as in M18. Therefore, we suspect that the difference in the results may be due to that [65] performed non-relativistic hydrodynamic simulations with an initial jet velocity of 0.1c, whereas our simulations (as well as M18) have used SRHD simulations (our initial jet velocity is set by $\beta\gamma = 0.6$, corresponding to $v \sim 0.5c$). Thus for the same jet luminosity, their jets are relatively denser ($\rho_{\text{jet}}/\rho_{\text{amb}} \sim 0.1$) and slower, which have higher momentum and tend to penetrate the disk. On the other hand, our relativistic jets are lighter ($\rho_{\text{jet}}/\rho_{\text{amb}} = 10^{-3}$) and faster, and hence are easier to dissipate due to the interaction with the dense disk. Of course, the true initial jet velocity and density contrast on the scale of injections are uncertain. However, our simulations show that the oblique-jet model could be plausible at least for some reasonable range of jet parameters, and that the range of jet luminosity allowed is dependent upon the details of how the jet injections are modeled.

Our simulations demonstrate that it is plausible to relieve the assumption of jet inclinations in terms of forming symmetric Galactic bubbles. However, we stress that there are several differences between this work and previous leptonic jet models that have assumed vertical jets [30, 84, 85, 87, 89]. In the previous leptonic jet models, the required jet power is near-Eddington, and thus the dissipation within the disk should be minor. Subsequently, the bubbles are formed from the lateral expansion when the ram pressure of the jets balances the external pressure, similar to the formation of cocoons of radio galaxies [e.g., 5, 12]. Because it takes only $\sim 2 - 3$ Myr for the Galactic bubbles to form, the advantage is that the jets could transport the CRe before they cool and reproduce the uniformly hard gamma-ray spectrum [88, 89]. The time scales and energetics are consistent with those inferred from elevated ionization signatures in the Magellanic Stream [8]. The drawback, though, is that it requires the jets to be perpendicular to the Galactic plane, which is either coincidental or requires efficient alignment between the black hole spin and the Galactic disk [e.g., 27]. On the other hand, if the jets were initially tilted with respect to the rotational axis of the Galaxy, then significant jet dissipation would be required to turn the kinetic energy of the jets into thermal energy. In this scenario, the bubbles are then inflated due to their internal pressure rather than the ram pressure. The advantages of the oblique-jet scenario are that it relaxes the assumption about the jet direction, and that only a moderate jet power is required (though the jet power is not uniquely determined, as influenced by the exact Galactic halo profiles used as well as numerical resolution as discussed in the last paragraph). Since it takes ~ 12 Myr for the bubbles to form, which is greater than the CRe cooling times, it remains to be seen whether the spatially uniform hard CR spectrum could be explained by taking into account turbulence re-acceleration within the bubbles.

[90] proposed that the *Fermi* bubbles are the product of a forward shock driven by a past jet source at the GC vertical to the Galactic plane. This model supports the idea that the *Fermi* bubbles are directly linked to the

dynamical impact of the jet event that imparts significant energy into the surrounding medium. The forward shock, in this scenario, sweeps up and heats the interstellar gas, creating the X-shaped structure near the GC as observed by ROSAT [7]. Following this line of reasoning, the eROSITA bubbles ought to be interpreted as a phenomenon unrelated to the *Fermi* bubbles, possibly attributed to a prior energetic outburst. This perspective is different from this work and previous leptonic jet models [89] that seek to explain both the *Fermi* and eROSITA bubbles as driven by a single event.

V. CONCLUSIONS

In this work, we introduce a thin, dense disk composed of clumpy ISM to stall and thermalize the oblique jets for an outburst event from the central SMBH in the Milky Way Galaxy 12 Myrs ago. We investigate the properties of the Galactic bubbles and the microwave haze using 3D SRHD simulations of CR jet injections from the SMBH assuming the leptonic model. The important findings are summarized as follows.

- The development of the expanding forward-reverse shock pair is always associated with the dense disk. In the absence of the disk, the reverse shock is absent, indicating the inclusion of the disk is critical for forming the innermost bubbles.
- The forward-reverse shock pair heats the turbulent plasma considerably (~ 2 keV). There exists a dense shell immediately downstream of the reverse shock, a situation reminiscent of a supernova shell.
- eROSITA bubbles coincide with the forward shock front originally driven by short-lived bipolar jets for a duration of 0.12 Myr, where the bubbles later significantly expanded into the stratified atmosphere to reach the present height of 12 kpc. The overall extent of the simulated X-ray bubbles is comparable to that of the eROSITA bubbles, though not as limb-brightened. Future models including shock-accelerated CRs may help to resolve this issue by increasing the compressibility of the fluid and enhancing the thermal Bremsstrahlung emissivity at the edge of the X-ray bubbles.
- Downstream of the reverse shock is filled with hot (~ 2 keV) and highly turbulent plasma brought from the disk. The interface between the downstream materials of reverse and forward shocks lies a contact discontinuity, which corresponds to the edge of the *Fermi* bubbles. The surface of the simulated bubbles is not as smooth as the observed ones; the inclusion of magnetic fields in the future may help suppress the instabilities at the bubble surface due to the magnetic draping effect.
- Assuming a power-law CRe energy spectrum ranging from 0.5 MeV to 560 GeV, where the spectrum is spatially uniform, we showed that the observed gamma-ray and microwave spectra can be simultaneously reproduced. The best-fit CRe power-law index is found to be 2.4 given our model assumptions. A spectral index of 2.2 could also be plausible if the amount of the microwave emission could be boosted by, e.g., a larger magnetic field than what was adopted, or additional contribution from secondary CR electrons.
- The elapsed time of 12 Myr is 10 times longer than the typical synchrotron and IC cooling time scale of high energy (~ 100 GeV) CRe. Thus, re-acceleration of CRe by shocks or turbulence must be considered in this model. Since the forward shock is rather far away from the gamma-ray bubbles, stochastic acceleration of CRs by turbulence appears to be more plausible. We will investigate the competition between stochastic acceleration and radiative cooling in future work.
- The Galactic bubbles are observed nearly symmetric about the Galactic plane albeit the bipolar jets are oblique with respect to the disk normal. We showed that the inclusion of the dense ISM disk (regardless of its clumpiness) is an essential ingredient for producing the symmetric Galactic bubbles when the jets are oblique. The influence of varied jet parameters is explored in detail in the Appendix A. An optimal combination of jet parameters is inferred; however, we caution that they could be influenced by the assumptions of our initial setup (e.g., constant height of the Galactic disk, lack of radial dependence of the Galactic halo profile, etc). Nevertheless, the broad agreement between the simulated and observed multi-wavelength features demonstrates that oblique failed jets are a plausible scenario for the formation of the Galactic bubbles, which relieves the caveat of earlier jet models where jets need to be vertical.

VI. ACKNOWLEDGEMENTS

The authors thank Mateusz Ruszkowski and Ellen G. Zweibel for insightful comments. We thank Henry Zovaro for discussions about the innermost bubbles during the final stages of this work. We thank Peter Predehl for providing the range of observed X-ray intensity in Fig. 8a. We further thank Chen Chun-Yen for providing the code module solving the cosmic ray convection equation. A part of the simulations are performed and analyzed using computing resources operated by the National Center for High-Performance Computing (NCHC). HYKY acknowledges support from Yushan Scholar Program of the Ministry of Education of Taiwan and Ministry of Science and Technology of Taiwan (MOST 109-2112-M-007-037-MY3; NSTC 112-2628-M-007-003-MY3). HS acknowledges funding support from the Yushan Scholar Program No. NTU-111V1201-5 and the NTU Academic Research-Career Development Project under Grant No. NTU-CDP-111L7779, sponsored by the Ministry of Education, Taiwan. This research is partially supported by the MOST under grants 107-2119-M-002-036-MY3 and NSTC 111-2628-M-002-005-MY4, and the NTU Core Consortium project under grants NTU-CC-108L893401 and NTU-CC-108L893402. TC acknowledges support from National Science and Technology Council (NSTC) under grants 111-2112-M-002-031.

Appendix A: jet parameter variations

Fig. 12 shows the simulated Galactic bubbles for a jet source with the same inclination angle of 45 degrees, but with different jet parameters, including gas temperature, density, and initial velocity. The parameter range explored in this study, including the fiducial run (C), is listed in Table II. The simulated gas pressure, temperature, and density distributions for these simulations are shown in Fig. 12. As discussed in the second paragraph of § IV, since the simulation results (i.e., whether jets could dissipate within the disk or not) are quite sensitive to the details of jet injections (e.g., size of the jet source, the average density of the disk, simulation resolution, etc), the range of jet parameters that could successfully produce symmetric bubbles may vary when the simulation details are different, and the readers should be cautious when quoting these parameters at face values. Also, because it is computationally expensive to cover all the possible parameters, the parameter space explored here is by no means complete. Instead, our main goal here is to show the qualitative trends when some of the parameters are adjusted.

We observe that higher density (F→C→E) or velocity (G→C→A) of the source can enhance the intensity of the shocks driven into the atmosphere. As a result, the post-shock region becomes hotter, and the bubbles show greater asymmetry around the GC. This results from the fact that the denser/faster jets are more likely to penetrate the thin disk in a short time, which prevents the jets from having enough time to interact with the disk and alter their orientations before being stretched vertically by the stratified atmosphere.

Also, we found that increasing the source temperature (B→C→D) not only improves the symmetry of the bubbles but also increases the temperature inside the bubbles at the present time. This result implies that a high-temperature source helps the jets ablate the clumpy dense gas away and pour into the atmosphere through the intercloud channels of the clumpy disk. In contrast, if the source temperature is not high enough, the jets cannot effectively ablate the high-density clouds within 12 Myr, resulting in the formation of asymmetric bubbles (case B).

Fig. 13, 14, 15, and 16 present the simulated distributions of gas, X-ray, γ -ray, and CRs for case C. Panels from left to right correspond to different jet inclination angles (0° , 45° , and 90°) relative to the z -axis. The overall morphology of the Galactic bubbles are similar among the three cases, indicating that the jet inclination angle has a negligible impact on the orientation of bubbles for the parameter space investigated in this study.

Despite the similarities of the bubble morphology, there are subtle differences of the observable features among the three cases. The bottom row of Fig. 13 shows that the larger the inclination angle, the denser the gas within the region between the outermost and innermost bubbles. In addition, the outermost bubbles produced by lying jets (rightmost column in Fig. 13) are the narrowest compared to others, resulting in shorter path lengths within the X-ray bright regions inside the outermost bubbles. Consequently, the X-ray bubbles arising from lying jets (the rightmost panel in Fig. 14) appear dimmer than the other two cases. However, as the extent of X-ray emission is larger than the Galactic bulge, please note that the simulated X-ray map may be different from the results obtained by the self-consistent Galactic model, involving radial variation of gravitational potential and the centrifugal force introduced by the rotation of the Galaxy.

The γ -ray maps (Fig. 15) reveal that the case produced by the 45° jets (middle panel) produces a γ -ray intensity distribution that is most consistent with the nearly flat distribution of the observed *Fermi* bubbles compared to other inclinations. Specifically, the case with 45° jets produces brighter γ -ray emission than the other two inclinations. This could be attributed to the two facts: (1) the lying jets provide less vertical gas velocity to carry the CRs away from the GC. Therefore, a significant portion of the injected CRs remains proximate to the GC at the present time, giving rise to dimmer γ -ray bubbles at high latitudes (rightmost panel in Fig. 15); (2) the vertical jets offer rapid vertical gas

TABLE II: The list of runs showing different injected jet parameters. The fiducial run (C) has been pointed out by an asterisk in the list.

	A	B	C*	D	E	F	G
$k_B T$ (MeV)	1.720	0.034	1.720	86.100	1.720	1.720	1.720
ρ (g/cm ³)	10 ⁻²⁶	10 ⁻²⁶	10 ⁻²⁶	10 ⁻²⁶	10 ⁻²⁵	10 ⁻²⁷	10 ⁻²⁶
$\beta\gamma$	1.20	0.60	0.60	0.60	0.60	0.60	0.30

flows before quenching, causing CRs to adiabatically expand (Fig. 16). As a result, the CR energy density decreases at high latitudes, leading to dimming of the γ -ray bubbles as well (leftmost panel in Fig. 15).

In summary, we conclude that the initial jet inclination angle has a minor influence on the ability to generate symmetric bubbles for the same set of jet parameters. However, tilted jets (e.g., 45°) could mitigate several issues: (1) preventing the outermost bubbles from being too narrow, which would dim the X-ray bubbles, (2) avoiding a significant pile-up of CRs near the GC, and (3) averting the dilution of CRs at high latitudes due to fast adiabatic expansion. The last two issues would result in non-uniform γ -ray intensity distributions, at odds with the observed *Fermi* bubbles.

Appendix B: Cosmic-Ray Implementation and Tests

This appendix provides an overview of the full implementation of cosmic rays (CRs) in GAMER in the non-relativistic limit, including the algorithm (B 1) and numerical tests (B 2 – B 4). See Section II for the simplification adopted in this paper for the relativistic case.

The governing equations of non-relativistic magnetohydrodynamics (MHD) with CR advection and anisotropic diffusion can be written as

$$\frac{\partial \rho}{\partial t} + \nabla \cdot (\rho \mathbf{v}) = 0, \quad (\text{B1a})$$

$$\frac{\partial \rho \mathbf{v}}{\partial t} + \nabla \cdot \left(\rho \mathbf{v} \mathbf{v} - \frac{\mathbf{B} \mathbf{B}}{4\pi} \right) + \nabla p_{\text{total}} = 0, \quad (\text{B1b})$$

$$\frac{\partial e}{\partial t} + \nabla \cdot \left[(e + p_{\text{total}}) \mathbf{v} - \frac{\mathbf{B}(\mathbf{B} \cdot \mathbf{v})}{4\pi} \right] = \nabla \cdot (\boldsymbol{\kappa} \cdot \nabla e_{\text{cr}}), \quad (\text{B1c})$$

$$\frac{\partial e_{\text{cr}}}{\partial t} + \nabla \cdot (e_{\text{cr}} \mathbf{v}) = -p_{\text{cr}} \nabla \cdot \mathbf{v} + \nabla \cdot (\boldsymbol{\kappa} \cdot \nabla e_{\text{cr}}), \quad (\text{B1d})$$

$$\frac{\partial \mathbf{B}}{\partial t} - \nabla \times (\mathbf{v} \times \mathbf{B}) = 0, \quad (\text{B1e})$$

where ρ is the gas mass density, $p_{\text{total}} = (\gamma_{\text{gas}} - 1)e_{\text{gas}} + (\gamma_{\text{cr}} - 1)e_{\text{cr}} + B^2/8\pi$ is the total pressure, \mathbf{v} is the velocity, \mathbf{B} is the magnetic field, $\boldsymbol{\kappa}$ is the diffusion tensor, and $e = 0.5\rho v^2 + e_{\text{gas}} + e_{\text{cr}} + B^2/8\pi$ is the total energy density. Here e_{gas} is the gas internal energy density, $\gamma_{\text{gas}} = 5/3$ is the adiabatic index of an ideal gas, and $\gamma_{\text{cr}} = 4/3$ is the effective adiabatic index of CRs in the relativistic limit [36]. $p_{\text{cr}} = (\gamma_{\text{cr}} - 1)e_{\text{cr}}$ and $p_{\text{gas}} = (\gamma_{\text{gas}} - 1)e_{\text{gas}}$ are respectively the CR and gas pressure. The CR diffusion term can be written as

$$\nabla \cdot (\boldsymbol{\kappa} \cdot \nabla e_{\text{cr}}) = \nabla \cdot (\kappa_{\parallel} \hat{\mathbf{b}} \hat{\mathbf{b}} \cdot \nabla e_{\text{cr}}) + \nabla \cdot [\kappa_{\perp} (\mathbf{I} - \hat{\mathbf{b}} \hat{\mathbf{b}}) \cdot \nabla e_{\text{cr}}], \quad (\text{B2})$$

where κ_{\parallel} and κ_{\perp} are the diffusion coefficients parallel and perpendicular to the magnetic field direction $\hat{\mathbf{b}}$, respectively [11], and \mathbf{I} is the identity matrix.

1. Algorithm

The CR module adopts the VL scheme [24, 81] and the constraint transport technique [23] for solving Eqs. B1a – B1e, supporting both piecewise linear and piecewise parabolic methods for data reconstruction [15, 80]. The CR equation (Eq. B1d) involves computing three terms: the advective flux $e_{\text{cr}} \mathbf{v}$, the adiabatic term $-p_{\text{cr}} \nabla \cdot \mathbf{v}$, and the

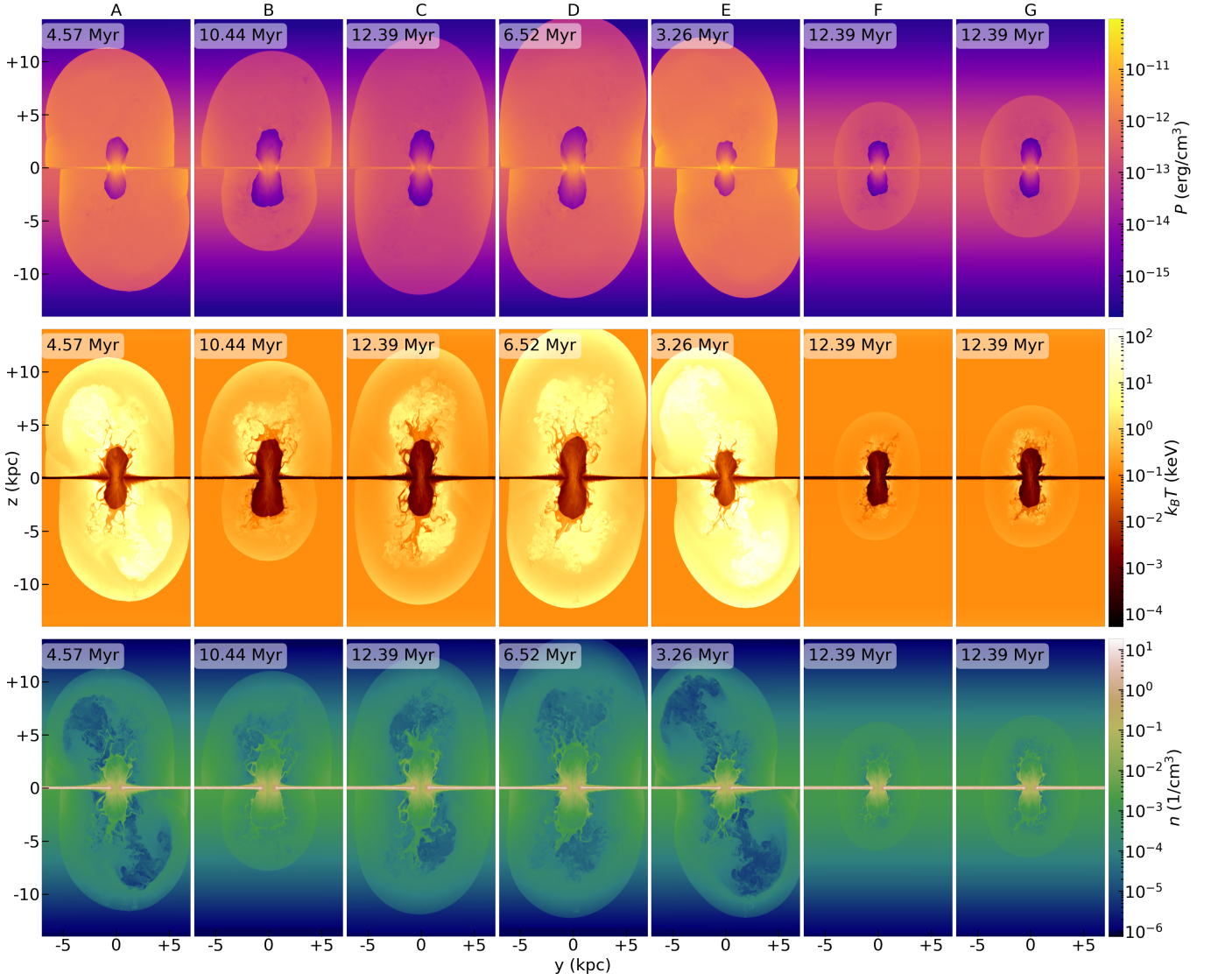


FIG. 12: Simulated gas distributions based on the parameters of the jet in Table. II for jet sources with the same inclination angle of 45° .

anisotropic diffusion flux $\kappa \cdot \nabla e_{\text{cr}}$. The advective flux is computed by regarding CR as a passive scalar advected along with the gas. The adiabatic term is computed as

$$-p_{\text{cr},i,j,k}^n \left[\frac{v_{i+1/2,j,k}^n - v_{i-1/2,j,k}^n}{\Delta x} + \frac{v_{i,j+1/2,k}^n - v_{i,j-1/2,k}^n}{\Delta y} + \frac{v_{i,j,k+1/2}^n - v_{i,j,k-1/2}^n}{\Delta z} \right], \quad (\text{B3})$$

where i, j, k are cell indices, n is the discrete time step, and $\Delta x, \Delta y, \Delta z$ are the cell sizes. The cell-interface velocity, for example, $v_{i-1/2,j,k}^n$, is computed by an upwind method,

$$v_{i-1/2,j,k}^n = \begin{cases} \frac{F_{i-1/2,j,k}^{n,\rho}}{\rho_{i-1,j,k}} & \text{if } F_{i-1/2,j,k}^{n,\rho} > 0, \\ \frac{F_{i-1/2,j,k}^{n,\rho}}{\rho_{i,j,k}} & \text{if } F_{i-1/2,j,k}^{n,\rho} \leq 0, \end{cases} \quad (\text{B4})$$

where $F_{i-1/2,j,k}^{n,\rho}$ is the cell-interface mass density flux between the cells $(i-1, j, k)$ and (i, j, k) .

We adopt a similar scheme as in Yang et al. [86] to compute the anisotropic diffusion flux in Eq. B2. For example, the flux at the $i+1/2$ cell interface at time n is given by

$$F_{i+1/2,j,k}^{n,\text{diffusion}} = -(\kappa_{\parallel} - \kappa_{\perp}) b_x \left[b_x \frac{\partial e_{\text{cr}}}{\partial x} + \overline{b_y} \frac{\partial e_{\text{cr}}}{\partial y} + \overline{b_z} \frac{\partial e_{\text{cr}}}{\partial z} \right] - \kappa_{\perp} \frac{\partial e_{\text{cr}}}{\partial x}, \quad (\text{B5})$$

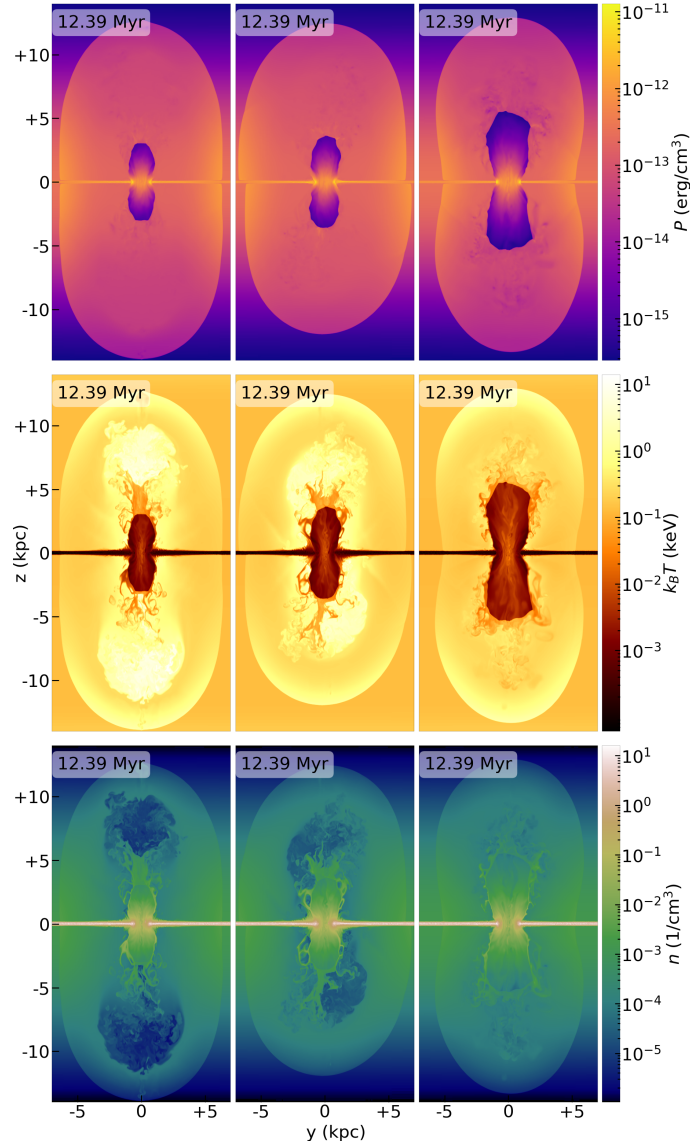


FIG. 13: Simulated gas distributions for the case C in Table. II with inclination angles 0° (left), 45° (middle), 90° (right) with respect to the z -axis.

$$b_x = b_{x,i+1/2,j,k}^n, \quad (\text{B6})$$

$$\bar{b}_y = (b_{y,i,j-1/2,k}^n + b_{y,i+1,j-1/2,k}^n + b_{y,i,j+1/2,k}^n + b_{y,i+1,j+1/2,k}^n)/4, \quad (\text{B7})$$

$$\bar{b}_z = (b_{z,i,j,k-1/2}^n + b_{z,i+1,j,k-1/2}^n + b_{z,i,j,k+1/2}^n + b_{z,i+1,j,k+1/2}^n)/4, \quad (\text{B8})$$

$$\frac{\partial e_{\text{cr}}}{\partial x} = \frac{e_{\text{cr},i+1,j,k} - e_{\text{cr},i,j,k}}{\Delta x}, \quad (\text{B9})$$

$$\overline{\frac{\partial e_{\text{cr}}}{\partial y}} = L \left[L \left(\left. \frac{\partial e_{\text{cr}}}{\partial y} \right|_{i,j-1/2,k}, \left. \frac{\partial e_{\text{cr}}}{\partial y} \right|_{i,j+1/2,k} \right), L \left(\left. \frac{\partial e_{\text{cr}}}{\partial y} \right|_{i+1,j-1/2,k}, \left. \frac{\partial e_{\text{cr}}}{\partial y} \right|_{i+1,j+1/2,k} \right) \right], \quad (\text{B10})$$

$$\overline{\frac{\partial e_{\text{cr}}}{\partial z}} = L \left[L \left(\left. \frac{\partial e_{\text{cr}}}{\partial z} \right|_{i,j,k-1/2}, \left. \frac{\partial e_{\text{cr}}}{\partial z} \right|_{i,j,k+1/2} \right), L \left(\left. \frac{\partial e_{\text{cr}}}{\partial z} \right|_{i+1,j,k-1/2}, \left. \frac{\partial e_{\text{cr}}}{\partial z} \right|_{i+1,j,k+1/2} \right) \right], \quad (\text{B11})$$

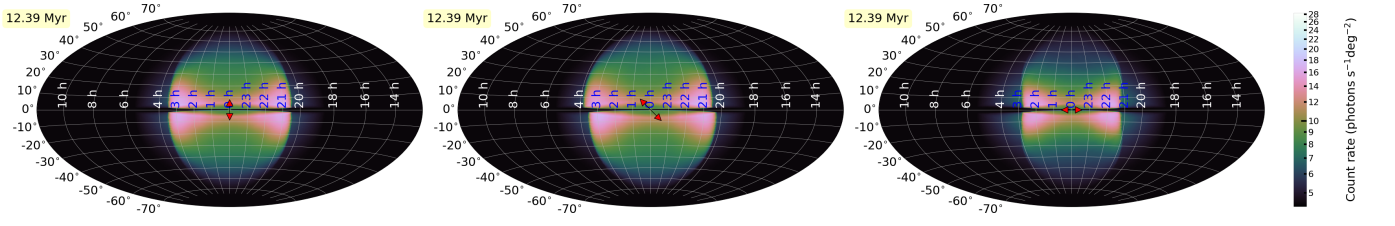


FIG. 14: Simulated X-ray bubbles for the case C in Table. II with inclination angles 0° (left), 45° (middle), 90° (right) with respect to the z -axis.

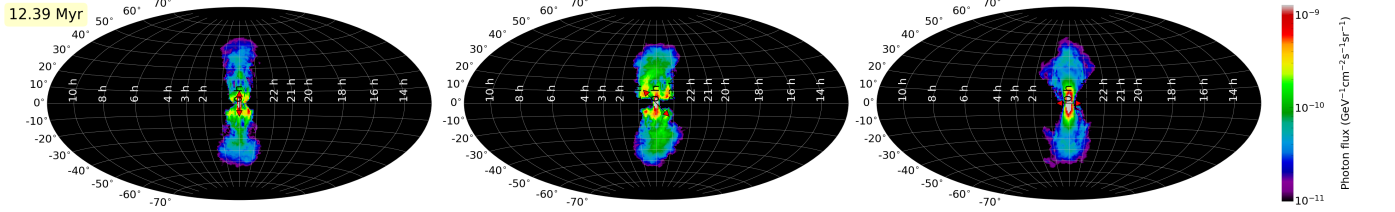


FIG. 15: Simulated γ -ray bubbles for the case C in Table. II with inclination angles 0° (left), 45° (middle), 90° (right) with respect to the z -axis.

where the diffusion coefficient κ is taken to be a constant. L is a slope limiter, for which we adopt the monotonized central limiter,

$$L(a, b) = \text{minmod} \left[2\text{minmod}(a, b), \frac{a + b}{2} \right], \quad (\text{B12})$$

$$\text{minmod}(a, b) = \begin{cases} \min(a, b) & \text{if } a, b > 0, \\ \max(a, b) & \text{if } a, b < 0, \\ 0 & \text{if } ab \leq 0. \end{cases} \quad (\text{B13})$$

We add the CR diffusion flux to the CR advective flux and the total energy flux when updating e_{cr} and e in Eqs.

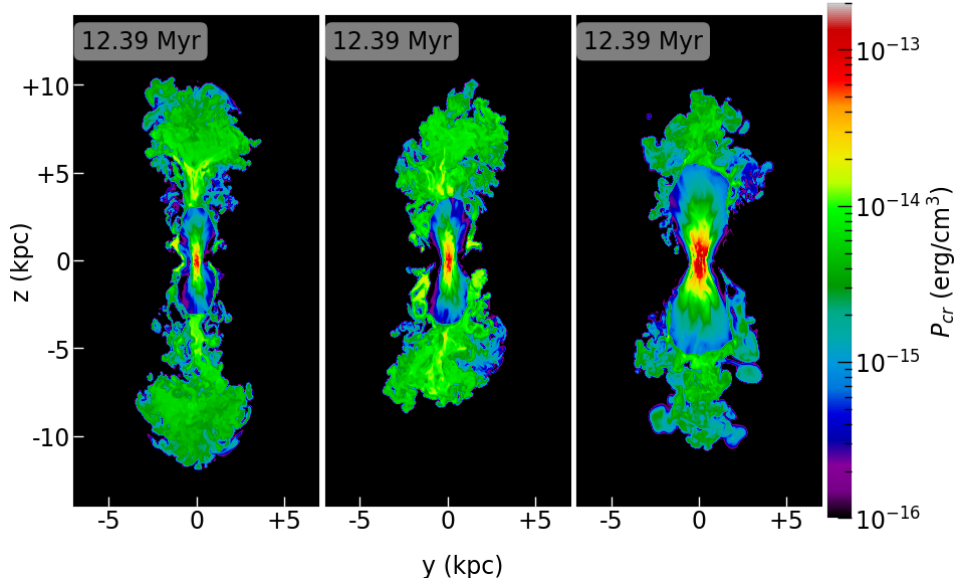


FIG. 16: Simulated CR distributions for the case C in Table. II with inclination angles 0° (left), 45° (middle), 90° (right) with respect to the z -axis.

B1c and B1d in a conservative fashion. All CR terms are incorporated into both the half- and full-time-step updates in the VL scheme, which is necessary to preserve second-order accuracy (see Section B 2).

The simulation time-step Δt must satisfy the following Courant–Friedrichs–Lewy (CFL) condition,

$$\Delta t \leq C_{\text{CFL}} \frac{\min [\Delta x^2, \Delta y^2, \Delta z^2]}{\max (\kappa_{\parallel}, \kappa_{\perp})}, \quad (\text{B14})$$

where C_{CFL} is the safety factor with a default value of 0.3.

By taking advantage of the flexibility and extensibility of GAMER, the CR module directly inherits the AMR structure and the hybrid MPI/OpenMP/GPU parallelization framework from the previous non-relativistic MHD and special-relativistic hydrodynamics implementations [78, 91]. Especially, the CPU/GPU integration infrastructure in GAMER allows the same source codes to be used for CPU-only and GPU-accelerated computations, avoiding redundant code development and simplifying code maintenance.

2. Linear Sound Wave Test

We use a linear sound wave to validate the coupling between CRs and gas and to measure the error convergence rate [64]. Small perturbations $\delta\rho$, δp_{gas} , δp_{cr} , and δv satisfying

$$\frac{\delta\rho}{\rho_0} = \frac{\delta p_{\text{gas}}}{\gamma_{\text{gas}} p_{\text{gas},0}} = \frac{\delta p_{\text{cr}}}{\gamma_{\text{cr}} p_{\text{cr},0}} = \frac{\delta v}{c_s} \quad (\text{B15})$$

are added to a homogeneous background $\rho_0 = 1$, $p_{\text{gas},0} = 1$, $p_{\text{cr},0} = 1$, and $v_0 = 1$, with $\delta\rho/\rho_0 = 10^{-6}$ to avoid any non-linear effect. Neither magnetic field nor CR diffusion is included in this test. The effective sound speed c_s is given by

$$c_s = \sqrt{\frac{\gamma_{\text{gas}} p_{\text{gas},0} + \gamma_{\text{cr}} p_{\text{cr},0}}{\rho_0}}. \quad (\text{B16})$$

The periodic computational domain is $\{x, y, z\} \in [0, 1]$ with a uniform resolution of $N = 32\text{--}512$ cells along each dimension. The sound wave travels along the diagonal direction with a wavelength of $1/\sqrt{3}$.

Fig. 17 compares the simulation results and the analytical solution with $N = 128$ after evolving for one period (left panel) and shows the L1-norm error as a function of N (right panel). Simulation data agree well with the analytical solution and achieve second-order accuracy.

3. Shock Tube Test

The shock tube problem provides a standard test for nonlinear evolution and shock capturing in computational hydrodynamics. For a hybrid fluid comprising gas and CRs, an analytical solution has been derived by Pfrommer et al. [59]. We perform one-dimensional simulations in a computational domain $x \in [0, 1]$ with outflow boundary conditions and a uniform resolution of $N = 1024$ cells. The left state of the fluid variables ($0 < x < 0.5$) is initialized as $\rho_L = 1.0$, $\mathbf{v}_L = 0.0$, $p_{\text{gas},L} = 6.7 \times 10^4$, and $p_{\text{cr},L} = 1.3 \times 10^5$; the right state ($0.5 \leq x < 1$) is initialized as $\rho_R = 0.2$, $\mathbf{v}_R = 0.0$, $p_{\text{gas},R} = 2.4 \times 10^2$, and $p_{\text{cr},R} = 2.4 \times 10^2$. Neither magnetic field nor CR diffusion is included in this test.

Fig. 18 shows the simulation results and the analytical solution at $t = 4.4 \times 10^{-4}$. The simulation results match well with the analytical solution, including the rarefaction wave, the contact discontinuity, and the shock.

4. Ring Test for Anisotropic CR Diffusion

The ring test simulates the anisotropic CR diffusion along a circular magnetic field [33, 58, 70, 86]. To simulate pure CR diffusion, all the fluid variables except for e_{cr} are fixed, $\mathbf{v} = 0.0$, and the adiabatic term $-p_{\text{cr}} \nabla \cdot \mathbf{v}$ is ignored. The magnetic field is set to $\mathbf{B} = (-y/r, x/r, 0)$ with $r = \sqrt{x^2 + y^2}$. The CR energy density is initialized as

$$e_{\text{cr}}(x, y) = \begin{cases} 12 & \text{if } 0.5 < r < 0.7 \text{ and } |\phi| \leq \frac{\pi}{12}, \\ 10 & \text{otherwise,} \end{cases} \quad (\text{B17})$$

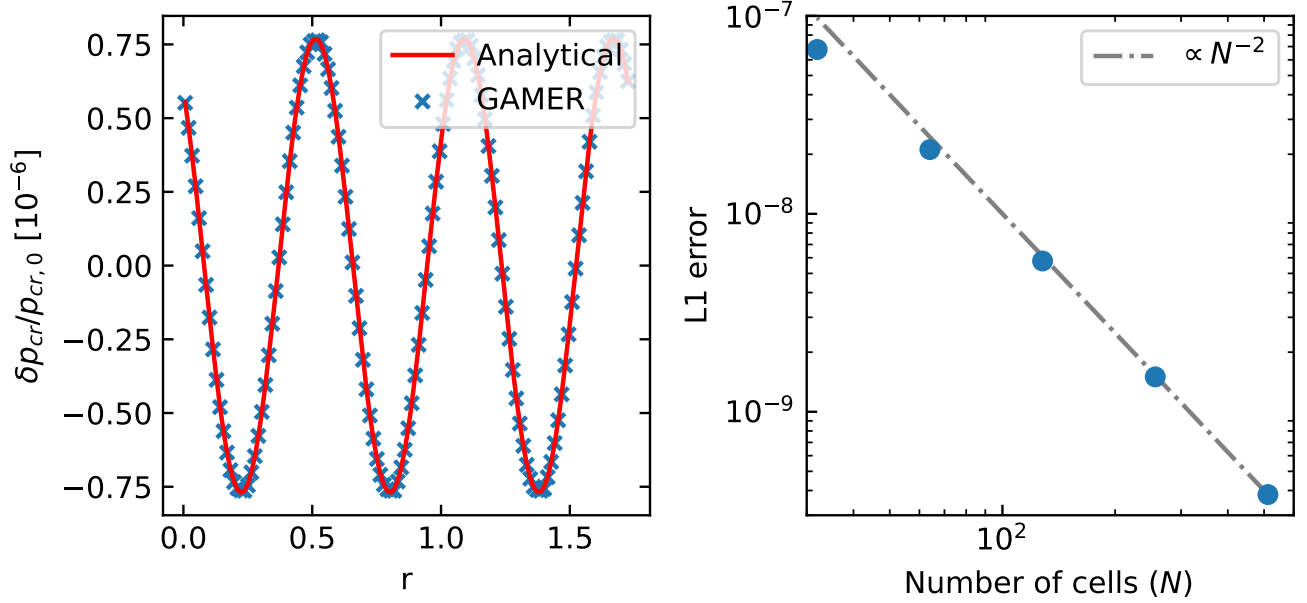


FIG. 17: CR linear sound wave test. The left panel shows the CR pressure perturbation in the diagonal direction after evolving for one period with $N = 128$. Crosses are the simulation data and the solid line shows the analytical solution. The right panel shows the L1 error, demonstrating second-order accuracy.

where $\phi = \text{atan2}(y, x)$ is the azimuthal angle. The diffusion coefficients are $\kappa_{\parallel} = 0.05$ and $\kappa_{\perp} = 0.0$. The analytical solution at time t is given by

$$e_{\text{cr}}(x, y, t) = \begin{cases} 10 + \text{Erfc} \left[\left(\phi - \frac{\pi}{12} \right) \frac{r}{\sqrt{4t\kappa_{\parallel}}} \right] - \text{Erfc} \left[\left(\phi + \frac{\pi}{12} \right) \frac{r}{\sqrt{4t\kappa_{\parallel}}} \right] & \text{if } 0.5 < r < 0.7, \\ 10 & \text{otherwise,} \end{cases} \quad (\text{B18})$$

where $\text{Erfc}(x)$ is the complementary error function. The computation domain is $\{x, y\} \in [-1, 1]$ with a uniform resolution of 256^2 cells.

Fig. 19 plots the simulation results at $t = 0, 0.1$, and 200 , showing good agreement with the analytical solutions. For the long-term solution at $t = 200$, diffusion along the azimuthal direction results in a homogeneous distribution of CRs within the ring, despite a small amount of numerical diffusion perpendicular to the magnetic field even with $\kappa_{\perp} = 0.0$ due to Cartesian grids.

-
- [1] Ackermann, M., Albert, A., Atwood, W. B., et al. 2014, *The Astrophysical Journal*, 793, 64, doi: 10.1088/0004-637x/793/1/64
 - [2] Ade, P. A. R., Aghanim, N., Arnaud, M., et al. 2013, *Astronomy & Astrophysics*, 554, A139, doi: 10.1051/0004-6361/201220271
 - [3] Arnaud, K. A. 1996, in *Astronomical Society of the Pacific Conference Series*, Vol. 101, *Astronomical Data Analysis Software and Systems V*, ed. G. H. Jacoby & J. Barnes, 17
 - [4] Atwood, W. B., Abdo, A. A., Ackermann, M., et al. 2009, *The Astrophysical Journal*, 697, 1071, doi: 10.1088/0004-637x/697/2/1071
 - [5] Begelman, M. C., & Cioffi, D. F. 1989, *ApJ*, 345, L21, doi: 10.1086/185542
 - [6] Berkhuisen, E. M., Haslam, C., & Salter, C. 1971, *Astronomy and Astrophysics*, 14, 252
 - [7] Bland-Hawthorn, J., & Cohen, M. 2003, *Astrophys. J.*, 582, 246, doi: 10.1086/344573
 - [8] Bland-Hawthorn, J., Maloney, P. R., Sutherland, R., et al. 2019, *Astrophys. J.*, 886, 45, doi: 10.3847/1538-4357/ab44c8
 - [9] Blitz, L., & Robishaw, T. 2000, 541, 675, doi: 10.1086/309457
 - [10] Blumenthal, G. R., & Gould, R. J. 1970, *Reviews of Modern Physics*, 42, 237, doi: 10.1103/revmodphys.42.237
 - [11] Braginskii, S. I. 1965, *Reviews of Plasma Physics*, 1, 205

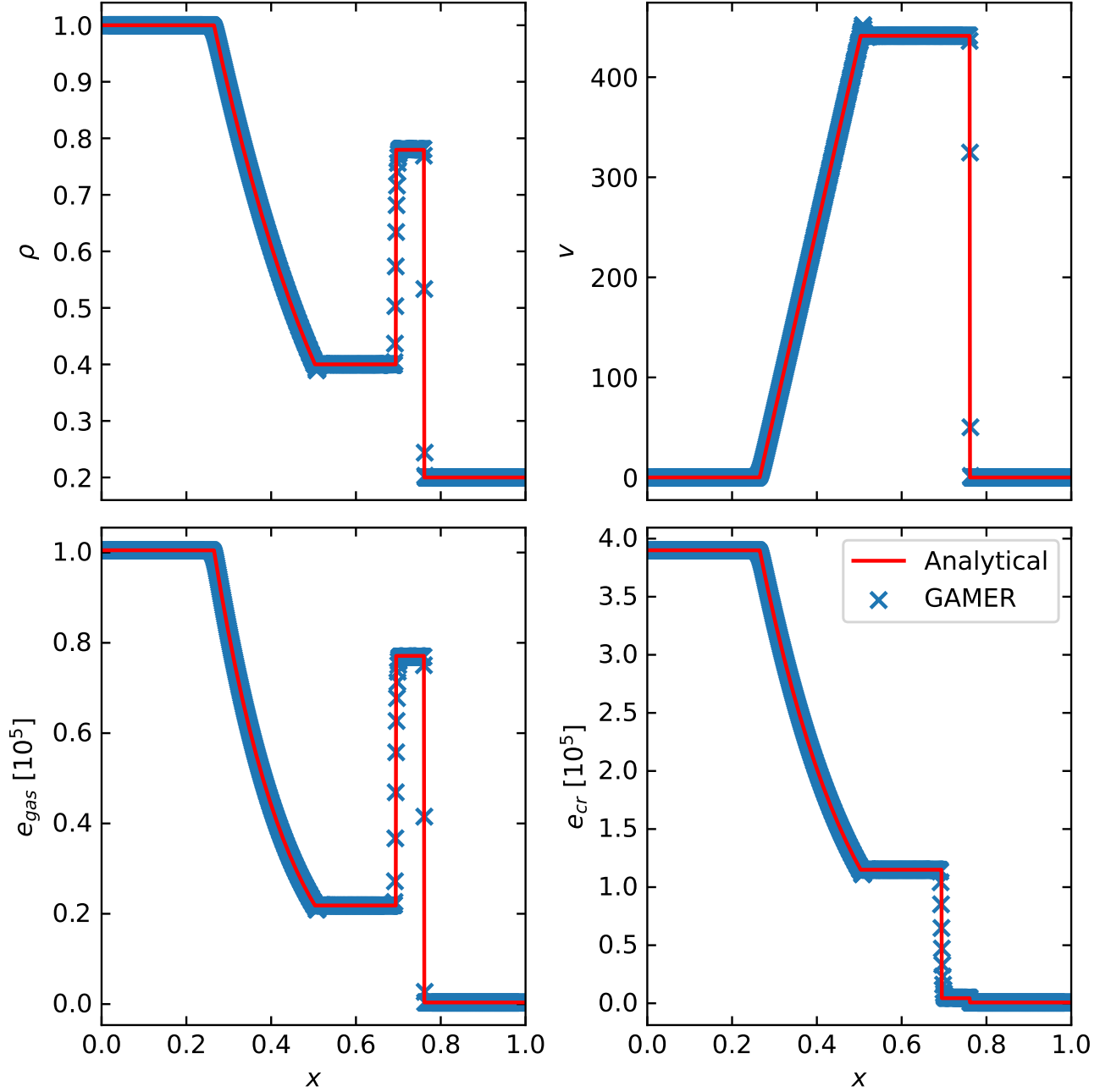


FIG. 18: CR shock tube test. It compares the gas mass density (top left), velocity (top right), gas internal energy density (bottom left), and CR energy density (bottom right) between the simulation results (crosses) and the analytical solution (solid lines).

- [12] Bromberg, O., Nakar, E., Piran, T., & Sari, R. 2011, *The Astrophysical Journal*, 740, 100, doi: 10.1088/0004-637X/740/2/100
- [13] Carretti, E., Crocker, R. M., Staveley-Smith, L., et al. 2013, *Nature*, 493, 66, doi: 10.1038/nature11734
- [14] Cecil, G., Bland-Hawthorn, J., Veilleux, S., & Filippenko, A. V. 2001, *The Astrophysical Journal*, 555, 338, doi: 10.1086/321481
- [15] Colella, P., & Woodward, P. R. 1984, *Journal of Computational Physics*, 54, 174, doi: 10.1016/0021-9991(84)90143-8
- [16] Crocker, R. M., & Aharonian, F. 2011, *Phys. Rev. Lett.*, 106, 101102, doi: 10.1103/PhysRevLett.106.101102
- [17] Crocker, R. M., Bicknell, G. V., Taylor, A. M., & Carretti, E. 2015, *Astrophys. J.*, 808, 107, doi: 10.1088/0004-637X/808/2/107

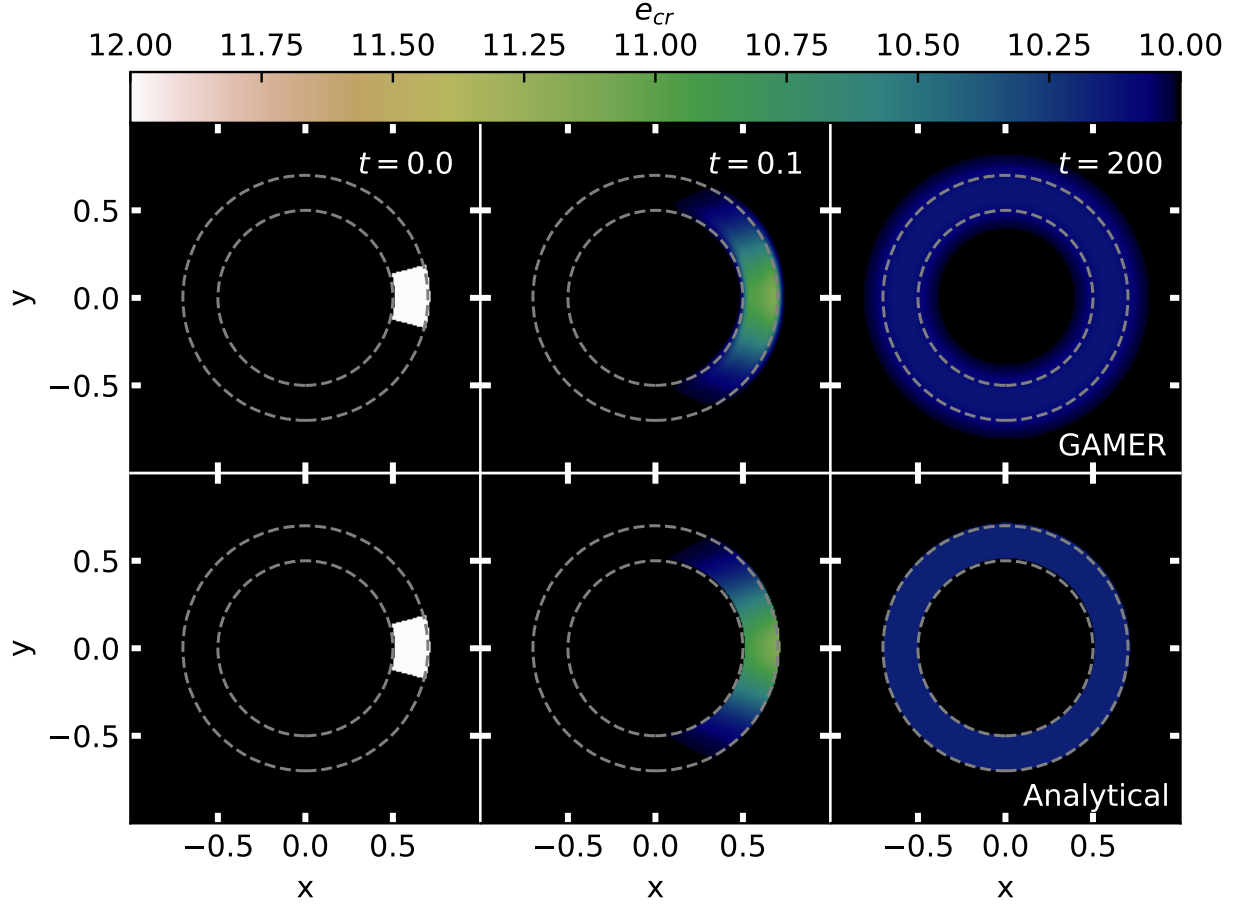


FIG. 19: CR ring test for anisotropic diffusion along a circular magnetic field. The top and bottom rows show the simulation results and the analytical solutions of CR energy density, respectively. Columns from left to right correspond to different simulation times: $t = 0, 0.1$, and 200 . The dashed circles with $r = 0.5$ and 0.7 enclose the region where diffusion occurs.

- [18] Crocker, R. M., Jones, D. I., Melia, F., Ott, J., & Protheroe, R. J. 2010, *Nature*, 463, 65, doi: 10.1038/nature08635
- [19] Das, K. K., Zucker, C., Speagle, J. S., et al. 2020, *Monthly Notices of the Royal Astronomical Society*, 498, 5863, doi: 10.1093/mnras/staa2702
- [20] Dobler, G., & Finkbeiner, D. P. 2008, *The Astrophysical Journal*, 680, 1222, doi: 10.1086/587862
- [21] Dopita, M. A., Shastri, P., Davies, R., et al. 2015, *The Astrophysical Journal Supplement Series*, 217, 12, doi: 10.1088/0067-0049/217/1/12
- [22] Dutta, R., Sharma, P., Sarkar, K. C., & Stone, J. M. 2023, arXiv e-prints, arXiv:2401.00446, doi: 10.48550/arXiv.2401.00446
- [23] Evans, C. R., & Hawley, J. F. 1988, *Astrophys. J.*, 332, 659, doi: 10.1086/166684
- [24] Falle, S. A. E. G. 1991, *Monthly Notices of the Royal Astronomical Society*, 250, 581, doi: 10.1093/mnras/250.3.581
- [25] Federrath, C., Roman-Duval, J., Klessen, R. S., Schmidt, W., & Low, M.-M. M. 2010, *Astronomy and Astrophysics*, 512, A81, doi: 10.1051/0004-6361/200912437
- [26] Ferrière, K. M. 2001, *Rev. Mod. Phys.*, 73, 1031, doi: 10.1103/revmodphys.73.1031
- [27] Fiacconi, D., Sijacki, D., & Pringle, J. E. 2018, *MNRAS*, 477, 3807, doi: 10.1093/mnras/sty893
- [28] Gallimore, J. F., Axon, D. J., O'Dea, C. P., Baum, S. A., & Pedlar, A. 2006, *The Astronomical Journal*, 132, 546, doi: 10.1086/504593
- [29] Greulich, J., & Putman, M. E. 2009, 696, 385, doi: 10.1088/0004-637x/696/1/385
- [30] Guo, F., & Mathews, W. G. 2012, *The Astrophysical Journal*, 756, 181, doi: 10.1088/0004-637x/756/2/181
- [31] Guo, F., Mathews, W. G., Dobler, G., & Oh, S. P. 2012, *Astrophys. J.*, 756, 182, doi: 10.1088/0004-637x/756/2/182
- [32] Heywood, I., Camilo, F., Cotton, W. D., et al. 2019, *Nature*, 573, 235, doi: 10.1038/s41586-019-1532-5

- [33] Jiang, Y.-F., & Oh, S. P. 2018, *The Astrophysical Journal*, 854, 5, doi: 10.3847/1538-4357/aaa6ce
- [34] Johnston, K. V., Spergel, D. N., & Hernquist, L. 1995, *The Astrophysical Journal*, 451, 598, doi: 10.1086/176247
- [35] Jones, F. C. 1968, *Physical Review*, 167, 1159, doi: 10.1103/physrev.167.1159
- [36] Jubelgas, M., Springel, V., Enßlin, T., & Pfrommer, C. 2008, *A&A*, 481, 33, doi: 10.1051/0004-6361:20065295
- [37] Kaastra, J. S., & Mewe, R. 1993, *A&AS*, 97, 443
- [38] Kataoka, J., Sofue, Y., Inoue, Y., et al. 2018, *Galaxies*, 6, 27, doi: 10.3390/galaxies6010027
- [39] —. 2018, *Galaxies*, 6, 27
- [40] LaRocca, D. M., Kaaret, P., Kuntz, K., et al. 2020, *The Astrophysical Journal*, 904, 54
- [41] Lewis, G. M., & Austin, P. H. 2002, 1th Conference on Atmospheric Radiation
- [42] Li, Z., Morris, M. R., & Baganoff, F. K. 2013, *Astrophys. J.*, 779, 154, doi: 10.1088/0004-637X/779/2/154
- [43] Liedahl, D. A., Osterheld, A. L., & Goldstein, W. H. 1995, *ApJ*, 438, L115, doi: 10.1086/187729
- [44] Lyutikov, M. 2006, *Monthly Notices of the Royal Astronomical Society*, 367, 1594, doi: 10.1111/j.1365-2966.2006.10069.x
- [45] Mathews, W. G. 1971, *Astrophys. J.*, 165, 147, doi: 10.1086/150883
- [46] Mertsch, P., & Petrosian, V. 2019, *Astronomy & Astrophysics*, 622, A203, doi: 10.1051/0004-6361/201833999
- [47] Mertsch, P., & Sarkar, S. 2011, *Phys. Rev. Lett.*, 107, 091101, doi: 10.1103/PhysRevLett.107.091101
- [48] Mewe, R., Gronenschild, E. H. B. M., & van den Oord, G. H. J. 1985, *A&AS*, 62, 197
- [49] Miller, M. J., & Bregman, J. N. 2013, *The Astrophysical Journal*, 770, 118, doi: 10.1088/0004-637x/770/2/118
- [50] —. 2016, *The Astrophysical Journal*, 829, 9, doi: 10.3847/0004-637x/829/1/9
- [51] Morganti, R., Oosterloo, T., Oonk, J. B. R., Frieswijk, W., & Tadhunter, C. 2015, *Astronomy & Astrophysics*, 580, A1, doi: 10.1051/0004-6361/201525860
- [52] Mou, G., Yuan, F., Bu, D., Sun, M., & Su, M. 2014, *Astrophys. J.*, 790, 109, doi: 10.1088/0004-637X/790/2/109
- [53] Mukherjee, D., Bicknell, G. V., Wagner, A. Y., Sutherland, R. S., & Silk, J. 2018, *MNRAS*, 479, 5544, doi: 10.1093/mnras/sty1776
- [54] Narayanan, S. A., & Slatyer, T. R. 2017, *Monthly Notices of the Royal Astronomical Society*, 468, 3051, doi: 10.1093/mnras/stx577
- [55] Note1. ????
- [56] Note2. ????
- [57] Panopoulou, G. V., Dickinson, C., Readhead, A. C. S., Pearson, T. J., & Peel, M. W. 2021, *The Astrophysical Journal*, 922, 210, doi: 10.3847/1538-4357/ac273f
- [58] Parrish, I. J., & Stone, J. M. 2005, *The Astrophysical Journal*, 633, 334, doi: 10.1086/444589
- [59] Pfrommer, C., Springel, V., Enßlin, T. A., & Jubelgas, M. 2006, *Monthly Notices of the Royal Astronomical Society*, 367, 113, doi: 10.1111/j.1365-2966.2005.09953.x
- [60] Ponti, G., Hofmann, F., Churazov, E., et al. 2019, *Nature*, 567, 347, doi: 10.1038/s41586-019-1009-6
- [61] Porter, T. A., Jóhannesson, G., & Moskalenko, I. V. 2017, *The Astrophysical Journal*, 846, 67, doi: 10.3847/1538-4357/aa844d
- [62] Predehl, P., Sunyaev, R. A., Becker, W., et al. 2020, *Nature*, 588, 227, doi: 10.1038/s41586-020-2979-0
- [63] Predehl, P., Andritschke, R., Arefiev, V., et al. 2021, *Astronomy & Astrophysics*, 647, A1, doi: 10.1051/0004-6361/202039313
- [64] Rasera, Y., & Chandran, B. 2008, *The Astrophysical Journal*, 685, 105, doi: 10.1086/591012
- [65] Sarkar, K. C., Mondal, S., Sharma, P., & Piran, T. 2023, *The Astrophysical Journal*, 951, 36, doi: 10.3847/1538-4357/acd75d
- [66] Sarkar, K. C., Nath, B. B., & Sharma, P. 2015, *Monthly Notices of the Royal Astronomical Society*, 453, 3828, doi: 10.1093/mnras/stv1806
- [67] Schive, H.-Y., Tsai, Y.-C., & Chiueh, T. 2010, *The Astrophysical Journal Supplement Series*, 186, 457, doi: 10.1088/0067-0049/186/2/457
- [68] Schive, H.-Y., ZuHone, J. A., Goldbaum, N. J., et al. 2018, *Monthly Notices of the Royal Astronomical Society*, 481, 4815, doi: 10.1093/mnras/sty2586
- [69] Selig, M., Vacca, V., Oppermann, N., & Enßlin, T. A. 2015, *Astronomy & Astrophysics*, 581, A126, doi: 10.1051/0004-6361/201425172
- [70] Sharma, P., & Hammett, G. W. 2007, *Journal of Computational Physics*, 227, 123–142, doi: 10.1016/j.jcp.2007.07.026
- [71] Sofue, Y. 2000, *The Astrophysical Journal*, 540, 224
- [72] Strong, A. W., Moskalenko, I. V., & Ptuskin, V. S. 2007, *Annual Review of Nuclear and Particle Science*, 57, 285, doi: 10.1146/annurev.nucl.57.090506.123011
- [73] Su, M., & Finkbeiner, D. P. 2012, *The Astrophysical Journal*, 753, 61, doi: 10.1088/0004-637x/753/1/61
- [74] Su, M., Slatyer, T. R., & Finkbeiner, D. P. 2010, *The Astrophysical Journal*, 724, 1044, doi: 10.1088/0004-637x/724/2/1044
- [75] Synge, J. L. 1957, North-Holland Pub. Co.; Interscience Publishers
- [76] Taub, A. H. 1948, *Physical Review*, 74, 328, doi: 10.1103/PhysRev.74.328
- [77] Tepper-García, T., Bland-Hawthorn, J., & Sutherland, R. S. 2015, *The Astrophysical Journal*, 813, 94, doi: 10.1088/0004-637x/813/2/94
- [78] Tseng, P.-H., Schive, H.-Y., & Chiueh, T. 2021, *Monthly Notices of the Royal Astronomical Society*, 504, 3298, doi: 10.1093/mnras/stab1006
- [79] Valenti, E., Zoccali, M., Mucciarelli, A., et al. 2018, *A&AS*, 616, A83, doi: 10.1051/0004-6361/201832905

- [80] van Leer, B. 1979, *Journal of Computational Physics*, 32, 101, doi: 10.1016/0021-9991(79)90145-1
- [81] van Leer, B. 2006, 192
- [82] Wagner, A. Y., Bicknell, G. V., & Umemura, M. 2012, *The Astrophysical Journal*, 757, 136, doi: 10.1088/0004-637x/757/2/136
- [83] Yang, H.-Y., Ruszkowski, M., & Zweibel, E. 2018, *Galaxies*, 6, 29, doi: 10.3390/galaxies6010029
- [84] Yang, H.-Y. K., & Ruszkowski, M. 2017, *The Astrophysical Journal*, 850, 2, doi: 10.3847/1538-4357/aa9434
- [85] Yang, H.-Y. K., Ruszkowski, M., Ricker, P. M., Zweibel, E., & Lee, D. 2012, *The Astrophysical Journal*, 761, 185, doi: 10.1088/0004-637x/761/2/185
- [86] Yang, H. Y. K., Ruszkowski, M., Ricker, P. M., Zweibel, E., & Lee, D. 2012, *Astrophys. J.*, 761, 185, doi: 10.1088/0004-637X/761/2/185
- [87] Yang, H.-Y. K., Ruszkowski, M., & Zweibel, E. 2013, *Monthly Notices of the Royal Astronomical Society*, 436, 2734, doi: 10.1093/mnras/stt1772
- [88] —. 2023, *PoS, ECRS*, 023, doi: 10.22323/1.423.0023
- [89] Yang, H.-Y. K., Ruszkowski, M., & Zweibel, E. G. 2022, *Nature Astronomy*, doi: 10.1038/s41550-022-01618-x
- [90] Zhang, R., & Guo, F. 2020, *The Astrophysical Journal*, 894, 117, doi: 10.3847/1538-4357/ab8bd0
- [91] Zhang, U.-H., Schive, H.-Y., & Chiueh, T. 2018, *The Astrophysical Journal Supplement Series*, 236, 50, doi: 10.3847/1538-4365/aac49e
- [92] Zhu, Z., Li, Z., Morris, M. R., Zhang, S., & Liu, S. 2019, *Astrophys. J.*, 875, 44, doi: 10.3847/1538-4357/ab0e05
- [93] Zweibel, E. G. 2013, *Physics of Plasmas*, 20, 055501, doi: 10.1063/1.4807033